

Measurement of the Ratio G_E^n/G_M^n by the
Double-polarized ${}^2\text{H}(\vec{e}, e'\vec{n})$ Reaction

December 1, 2010

J.R.M. Annand (spokesperson & contact), D.J. Hamilton, D. Ireland,
R. Kaiser, K. Livingston, I.J.D. MacGregor, G. Rosner, B. Seitz, J. Sjögren
University of Glasgow, Glasgow G12 8QQ, UK.

B. Wojtsekhowski (spokesperson), K. Allada, A. Camsonne, J.P. Chen,
P. Degtyarenko, J. Gomez, O. Hansen, D. Higinbotham, C.W. de Jager,
M. Jones, J. LeRose, R. Michaels, L. Pentchev, S. Nanda, A. Saha
*Thomas Jefferson National Accelerator Facility, Newport News, VA 23606,
USA.*

N. Piskunov (spokesperson), S. Basylev, D. Kirillov, G. Meshcheryakov,
J. Mushinsky, A. Nagaytsev, I. Savin, I. Slepnev, V. Slepnev, I. Sitnik
Joint Institute for Nuclear Research, Dubna, Russian Federation.

G. De Cataldo, R. de Leo, L. Lagamba, S. Marrone, G. Simonetti, E. Nappi,
I.J. Vilaridi
INFN Bari and University of Bari, Bari, Italy.

D. Nikolenko, I. Rachek, Yu. Shestakov
Budker Institute, Novosibirsk, Russian Federation.

K. Aniol and D.J. Magaziotis
California State University, Los Angeles, CA 90032, USA.

G. B. Franklin, B. Quinn, R. Schumacher
Carnegie Mellon University, Pittsburgh, PA 15213, USA.

V. Bellini, A. Giusa, F. Mammoliti, F. Noto, G. Russo, M.L. Sperduto,
C.M. Sutura
INFN Catania and University of Catania, Catania, Italy.

W. Boeglin, P. Markowitz, J. Reinhold, M.M. Sargsian
Florida International University, Miami, FL 33199, USA

M. Aghasyan, E. de Sanctis, L. Hasch, L. Lucherini, M. Mirazita, S.A. Pereira,
P. Rossi
INFN, Laboratori Nazionali di Frascati, Frascati, Italy.

G. Ron
Hebrew University of Jerusalem, Jerusalem, Israel

B. Anderson, A.T. Katramatou, G.G. Petratos
Kent State University, Kent, OH 44242, USA.

A. Glamazdin, R. Pomatsalyuk
Kharkov Institute of Physics and Technology, Kharkov 61108, Ukraine.

R. Perrino
INFN Lecce, Lecce, Italy.

A. Pucket
Los Alamos National Laboratory, Los Alamos, NM 87545, USA.

K. Fissum
Lund University, Lund, Sweden.

S. Riordan
University of Massachusetts, Amherst MA 01003, USA.

W. Bertozzi, S. Gilad, A. Kelleher, V. Sulkosky
Massachusetts Institute for Technology, Cambridge, MA 02139, USA.

F. Cusanno
Technische Universität München, Garching 85748, Germany.

J. Calarco, W. Hersman, K. Slifer
University of New Hampshire, Durham, NH 03824, USA.

M. Khandaker, V. Punjabi
Norfolk State University, Norfolk, VA 23504, USA.

B. Vlahovic
North Carolina Central University, Durham, NC 03824, USA.

E. Cisbani, S. Frullani, F. Garibaldi
INFN Rome, gruppo collegato Sanità and Istituto Superiori di Sanità, Rome, Italy.

F. Meddi and G.M. Urciuoli
INFN Rome and University "La Sapienza", Rome Italy.

M. Capogni
INFN Rome, gruppo collegato Sanità and ENEA Casaccia, Rome, Italy.

A. D'Angelo, C. Schaerf, V. Vegna
INFN Sezione Roma Tor Vergata and Università di Roma Tor Vergata, Rome, Italy.

L. El Fassi, R. Gilman, G. Kumbartzki, R. Ransome, Y. Zhang
Rutgers, The State University of New Jersey, Piscataway, NJ 08854, USA.

F. Sabatie
CEA Saclay, Gif-sur-Yvette, France.

A. Sarty
St. Mary's University, Nova Scotia, B3H 3C3, Canada.

M. Olson
St. Norbert College, De Pere, WI 54115, USA.

O. Chen, N. Bubis, I. Korover, J. Lichtenstadt, E. Piasetzky, I. Pomerantz,
R. Shneor, I. Yaron
Tel Aviv University, Israel.

G. Cates, D. Day, C. Hanrrety, R. Lindgren, N. Liyanage, V. Nelyubin,
B. Norum, M. Shabestari
University of Virginia, Charlottesville, VA 22901, USA.

T. Averett, C. Perdrisat
College of William and Mary Williamsburg, VA 23185, USA.

S. Abrahamyan, S. Mayilyan, A. Shahinyan, H. Voskanyan
Yerevan Physics Institute, Yerevan, Armenia.

Abstract

A double polarized measurement of quasi-elastic electron scattering in the ${}^2\text{H}(\vec{e}, e'\vec{n})$ reaction is proposed at values of negative four-momentum transfer $Q^2 = 1.5, 2.0, 2.5, 3.0, 4.0$ (GeV/c) 2 . The ratio of electric to magnetic elastic form factors G_E^n/G_M^n will be extracted from the ratio of transverse and longitudinal components of the spin polarisation P_x/P_z which is transferred to the recoiling neutron from an incident, longitudinally polarized electron. The experiment will be performed in Hall-A of Jefferson Laboratory, as part of the “Super BigBite” programme to measure the four nucleon Sachs form factors, and will utilize many of the common components of the Super BigBite apparatus. Scattered electrons will be detected in the “BigBite” large acceptance spectrometer and recoiling neutrons in a polarimeter consisting of plastic-scintillator analyser and the “HCAL” hadron calorimeter. The “48D48” dipole will perform neutron spin precession and sweeping of charged background out of the neutron arm acceptance. The array of plastic scintillator bars, in which neutrons will scatter in order to analyse the incident spin orientation, will be a new component of the Super BigBite apparatus.. This experiment will complement experiments E02-013 and E12-09-016, where the struck neutron is polarized in the initial state in a ${}^3\vec{\text{He}}$ target. It employs an independent experimental technique to extract a fundamental observable which is highly challenging to measure. In addition the necessary corrections for bound-neutron effects and final state interactions in ${}^2\text{H}$ and ${}^3\text{He}$ will be rather different and in principle more straight forward for A=2 system. We estimate that the ratio G_E^n/G_M^n will be measured to 3 – 4% (statistical) precision up to 3 (GeV/c) 2 and 6% at 4 (GeV/c) 2 , which requires a total beam time of 1320 hr to measure the ratio and perform all necessary commissioning and calibration of apparatus.

Contents

0.1	Introduction	3
0.1.1	Physics Motivation	4
0.1.1.1	pQCD Scaling and Scaling Violations	5
0.1.1.2	Dyson-Schwinger Equation Calculations	6
0.1.1.3	Constituent Quark Models	6
0.1.1.4	Lattice QCD	8
0.1.1.5	Generalized Parton Distributions	9
0.1.1.6	Quark Orbital Angular Momentum	9
0.1.1.7	The Form Factors as a Hadronic Model Testing Ground	10
0.2	Observables and Previous Experiments to Access the Form Factors	11
0.2.1	Rosenbluth Separation	12
0.2.2	Double polarized measurements	12
0.2.2.1	Polarized Beam and Polarized Target	13
0.2.2.2	Polarized Beam and Recoil Polarimetry	13
0.2.3	Nucleon Polarimetry	14
0.2.3.1	Neutron Analysing Power at Several GeV/c	16
0.2.4	Previous Form Factor Measurements and Proposals	16
0.2.4.1	Unpolarized	16
0.2.4.2	Polarized Target	17
0.2.4.3	Recoil Polarimetry	17
0.2.5	New Elastic Form Factor Measurements at JLab.	18
0.2.5.1	Comparison of the Present Proposal to Hall-C Proposal PR-09-006	19
0.3	Experimental Method	21
0.3.1	The e' Detector BigBite	22
0.3.2	The Neutron Polarimeter	24
0.3.2.1	The Plastic Scintillator Analyser Array and Veto Detector	24
0.3.2.2	The GEM Charged Particle Tracker	25
0.3.2.3	The HCAL Hadron Calorimeter	25
0.3.2.4	The 48D48 Dipole	25

0.3.3	Kinematics	27
0.3.4	The Proposed Measurement of the $n - CH$ Analysing Power at JINR.	30
0.4	Determination of the Ratio G_E^n/G_M^n	30
0.4.1	Modelling the polarimeter	30
0.4.1.1	The Simulated Response of the Analyser Block	32
0.4.1.2	The Simulated Response of the Hadron Calorimeter HCAL	33
0.4.1.3	The Simulated Response of the Polarimeter	34
0.4.1.4	Determination of G_E^n/G_M^n from Simulated Azimuthal Asymmetries	36
0.4.2	Background Rates and the Trigger Rate	38
0.4.3	The Quasi-elastic Signal and Background Rejection	39
0.4.4	Systematic Uncertainties	43
0.5	Proposed Measurements	44
0.5.1	Counting Rate Estimates	44
0.5.2	Beam Time Request	46
0.6	Summary	46

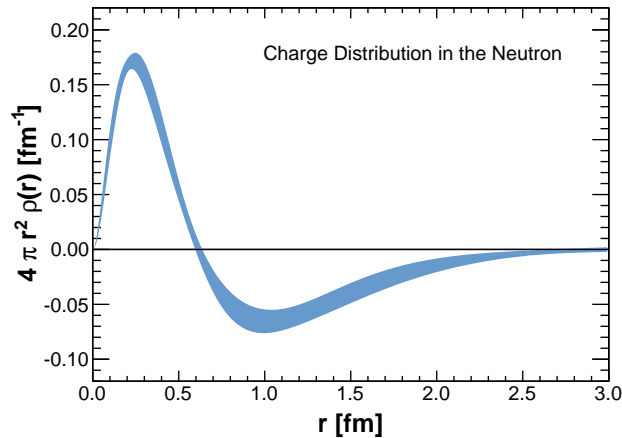


Figure 1: Radial dependence of the neutron charge density computed from the 2007 world data on G_E^n .

0.1 Introduction

The understanding of nucleon structure and the nature of quark confinement is one of the central goals facing nuclear physics today. Ninety nine per cent of the nucleon mass, is due to the kinetic and potential energy of the massless gluons and the essentially massless quarks, confined within the nucleon. Thus most of the mass of “everyday” matter is generated dynamically, rather than through the Higgs mechanism. At the $\sim fm$ scales typical of hadrons, quantum chromodynamics (QCD), the field theory describing the quark-gluon interaction, is too strong to be solved by perturbative methods (pQCD) and the understanding of non-perturbative QCD remains a pivotal area of theoretical physics.

Since the days of Hoffstadter [1], the elastic form factors have provided vital insight into nucleon structure. These are measured in electron scattering and at small values of Q^2 (the negative, squared, four momentum transfer) the Fourier transforms of the electric (G_E) and magnetic (G_M) form factors can be interpreted as the charge and magnetization densities respectively. Form factor measurements provided an early determination of the size of the proton and high precision studies of the proton remain a core activity of hadron physics. Neutron measurements are more difficult and consequently neutron data generally has poorer precision and a limited kinematic reach. Fig.6 is a representation of the charge density of the neutron computed from the 2007 world data set on G_E^n . The central core is positive, while the more diffuse outer region is negative, consistent with a proton-like core surrounded by a negative pion cloud. Several nucleon models incorporate the pion-cloud idea, which necessarily represents a five-quark state, a configuration that is suppressed when $Q^2 \gg \Lambda_{\text{QCD}}^2$. As Q^2 increases relativistic effects limit the degree to which form factors may be interpreted as Fourier transforms of densities but none the less attempts to account for relativity in the laboratory frame have been conducted [2, 3].

One of the critical factors driving progress in understanding nucleon structure is

the availability of high precision experimental results at the largest possible Q^2 . Pushing to higher values of Q^2 has immense potential to assess different nucleon structure models. At higher Q^2 the short-range behavior of the nucleon can be revealed, and the structure itself becomes simpler and easier to understand. The Q^2 dependence of G_E^p/G_M^p has generated more theoretical papers than any other result to come out of Jefferson Laboratory (JLab) and there is considerable anticipation regarding new results that push both G_E^p/G_M^p and G_E^n/G_M^n to higher values of Q^2 . Measurements of the elastic form factors remain a major source of information about quark distributions at small transverse distance scales. Indeed many theoretical approaches to understanding nucleon structure including, phenomenological models, analyses based on GPDs and lattice QCD calculations, require input and constraint from form-factor measurements.

The Super-Bigbite-Spectrometer (SBS) experimental programme already has three approved measurements of nucleon elastic form factors [4, 5, 6], which will use the results of E12-07-108 [7]. This will measure G_M^p up to 17.5 (GeV/c)^2 using the Hall-A HRS spectrometers to achieve a 1-2% measurement of the electron-proton elastic scattering cross section. Thus extraction of absolute values of G_M^n , G_E^p and G_E^n from ratio measurements will be possible. A major strength of the SBS programme in Hall-A is the ability to measure all of the ground-state electromagnetic form factors with sufficient accuracy and reach in Q^2 to tackle some of the most fundamental and topical questions in hadronic physics.

We propose to measure G_E^n/G_M^n to high precision for $Q^2 = 1.5 - 4.0 \text{ (GeV/c)}^2$, through the process ${}^2\text{H}(\vec{e}, e \vec{n})$. This will provide an independent measurement to E02-013 [8] and overlap in kinematic range with the new experiment E12-09-016 [4], both of which employ ${}^3\text{He}(\vec{e}, n)$. Existing ${}^2\text{H}(\vec{e}, e \vec{n})$ data [9] extend up to $Q^2 = 1.5 \text{ (GeV/c)}^2$. Neutron measurements are technically very challenging and must employ quasi-free scattering from nuclei, which introduces some uncertainty in extrapolation to the free-neutron case. Thus it is important to have different experimental techniques with different systematic effects and different nuclear targets with different binding and final state interaction effects. The present measurement will also improve significantly the precision of G_E^n/G_M^n in the several $(\text{GeV/c})^2$ domain. We refrain from attempting to push to higher values of Q^2 as the efficiency of the recoil polarimetry technique is rather uncertain for neutron momenta of several (GeV/c) . However in parallel we are setting up an experiment at Dubna to answer this technical question, with a view to possible future extensions of the kinematic range.

0.1.1 Physics Motivation

The study of the electromagnetic form factors remains central to the progress that is being made in understanding hadron structure. The results of [10] have stimulated a drive to progress our understanding of nucleon structure, as evidenced by more than 500 citations of the original paper.

Several theoretical approaches, which are outlined in the following subsections, have been taken to calculate the elastic form factors.

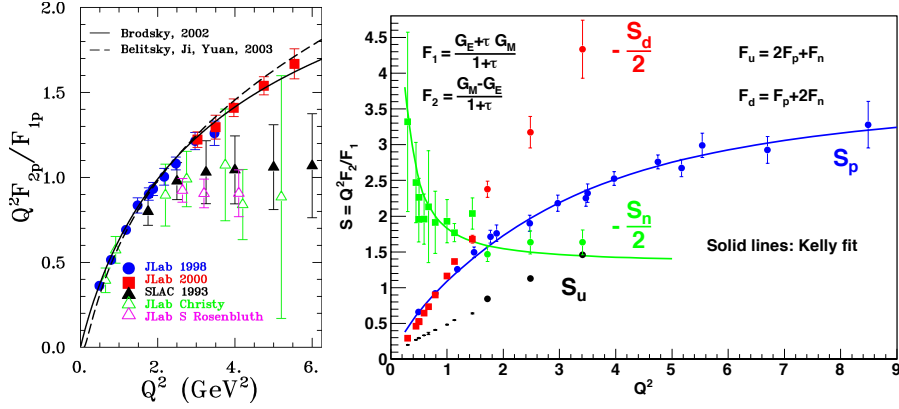


Figure 2: $Q^2 F_2/F_1$ as a function of Q^2 . Left: proton data derived from world double polarized measurements (red, blue) and Rosenbluth separation (green, magenta, black) compared to the theoretical predictions of Ref.[18]. Right: the fit of [20] to proton (blue) and neutron (green) world data. Also shown is a flavor decomposition with u (black) and d (red).

0.1.1.1 pQCD Scaling and Scaling Violations

The Sachs form factors G_E, G_M are linear combinations (Eq.3,4) of the fundamental Dirac (F_1 helicity conserving) and Pauli (F_2 helicity flip) form factors. At sufficiently high values of Q^2 , F_1 should scale as $1/Q^4$, while F_2 should scale as $1/Q^6$ [11] essentially on the basis of quark counting rules. After Ref.[10], it became clear that the proton F_2/F_1 did not scale as $1/Q^2$ as evident in Fig.2. The difference in apparent scaling behaviour of proton data derived from double-polarized measurements [12, 13, 14], as opposed to Rosenbluth separation of differential cross sections [15, 16, 17], is discussed in Sec.0.2. The apparent scaling behaviour of data obtained by Rosenbluth separation is now thought to be spurious.

A more recent pQCD calculation [18] relaxed the assumption [11] that the quarks move collinearly with the proton. It included components in the light-cone nucleon wave functions with a quark orbital angular momentum projection $L_z = 1$, equivalent to relaxing hadron helicity conservation, and obtained the scaling relation $F_2/F_1 \propto \ln^2(Q^2/\Lambda^2)/Q^2$, where Λ is a non-perturbative mass scale.

Agreement with the JLab double polarized G_E^p/G_M^p measurements is quite good up to about 6 (GeV/c)² (Fig.3) although newer data suggest a more gradual fall off with Q^2 . The implication of this scaling is that quark orbital angular momentum is playing an important dynamical role in the Q^2 -evolution of the proton form factors. At sufficiently high values of Q^2 one still expects that F_1/F_2 will scale as $1/Q^2$, but observation of the transition to this behaviour is beyond the reach of current experimental facilities. Fig.2 (left) [19] displays both proton and neutron results from JLab, along with an empirical fit to the data [20]. These have been combined to produce equivalent distributions for u and d quarks. Assuming negligible nucleon strange content the u, d quark form factors may be obtained from:

$$F_{1,2}^u(Q^2) = F_{1,2}^n + 2F_{1,2}^p \quad F_{1,2}^d(Q^2) = 2F_{1,2}^n + F_{1,2}^p \quad (1)$$

emphasising the importance of having both proton and neutron data, a major strength of the Hall-A SBS programme.

It is interesting that, although the nucleon data seem to be converging towards scaling behaviour, there is little hint of this in the flavor-separated distributions.

0.1.1.2 Dyson-Schwinger Equation Calculations

This technique, based on the infinite series of Dyson-Schwinger Equations (DSE) that interrelate the Green's functions of field theories [21], may have the potential to provide solutions to QCD in the non-perturbative regime with arbitrarily high accuracy. However in any practical calculation the series of DSE must be truncated, and some Ansätze must be employed to account for the omissions. Recent calculations explicitly describe the dynamical generation of the mass of constituent quarks, and show excellent agreement with lattice QCD results that necessarily assume large current-quark masses.

Using dressed quarks as the elementary degrees of freedom, the nucleon form factors may be calculated using a Poincaré covariant Faddeev equation [22]. This work also assumes that two of the quarks couple into a diquark. While still an approximation, the DSE/Faddeev approach is partly based on first principles. It is limited, however, in that precisely three constituent quarks are considered, so that for instance pion-cloud effects cannot be investigated. However, it is reasonable to assume the dominance of the 3-quark component of the wave function at relatively high values of Q^2 .

DSE/Faddeev calculations (Fig.3) have been made for both G_E^p/G_M^p and G_E^n/G_M^n . Proton curve fluctuations appear to be “unphysical” and the curve’s description of the data is poor. The neutron calculation is consistent with the available data.

At moderate values of Q^2 high precision measurements are well suited to investigate structural effects such as the di-quark. However the extraction of meaningful structure information will require $\sim 5\%$ experimental uncertainty. This proposal aims to make measurements of this quality.

0.1.1.3 Constituent Quark Models

Constituent Quark Models (CQM) have a long history of interpretation of the form-factor measurements that have come out of JLab. Even before [10] a relativistic CQM [30] predicted a strong decrease of G_E^p/G_M^p with Q^2 . Subsequently it was shown [31] that the decrease of G_E/G_M is associated with a violation of helicity conservation, or equivalently nonzero quark orbital angular momentum, and further work [26] using the so-called “light-front cloudy bag model” reproduced much of the form-factor data over a broad range of Q^2 .

A limitation that is inherent to CQM calculations is that they do not respect the chiral symmetry of the QCD Lagrangian. The “cloudy bag model” is an early example of a bag model that restores chiral symmetry. The breaking of chiral symmetry gives rise to the pions, so by including them, it is possible to restore

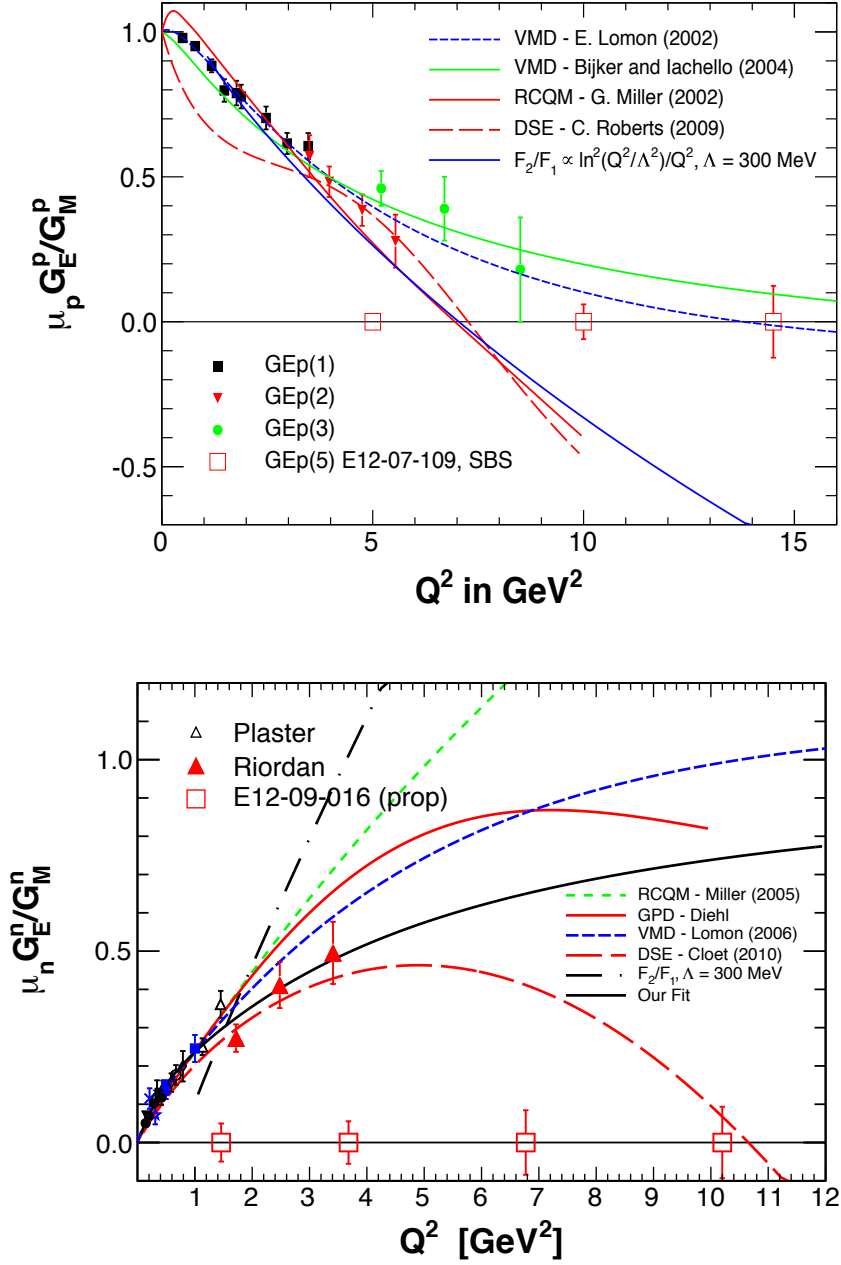


Figure 3: Form factor ratios G_E^n/G_M^n (right). On the top plot are shown the published G_E^p/G_M^p JLab results [12, 13, 14] and the projected results of GEp(5) [6]. On the bottom plot are shown previously published G_E^n/G_M^n data [9], the results of GEn(1) [8] and the projected results of GEn(2) [6]. The theoretical curves are as follows: VMD (blue dash) [23, 24]; VMD (green) [25]; RCQM (red) [26]; RCQM (green dash) [28]; DSE (proton) [27]; DSE (neutron) [22]; GPD (neutron) [29].

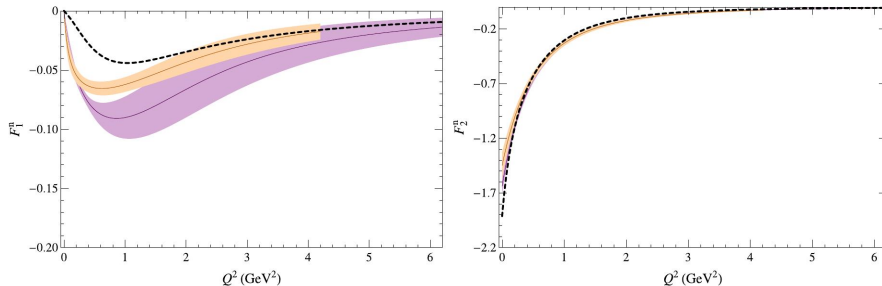


Figure 4: LQCD calculation [33] of neutron Dirac F_1 and Pauli F_2 form factors. The quenched approximation is shown in purple while dynamical calculations are in pink. The purple/pink shaded areas indicate the uncertainties in the calculation. The dashed line is derived from a fit [20] to the experimental data.

the symmetry of the theory. Inclusion of pions then leads to a pion cloud, which in turn governs certain aspects of the the low- Q^2 behavior of the form factor. Thus precise form factor measurements in this kinematic domain have immense potential to illuminate such fundamental structure phenomena.

With the interpretation of an appropriate model that respects both Poincaré invariance and chiral symmetry, the importance of both quark orbital angular momentum and the pion cloud is emphasised. The light-front cloudy bag model, is in quite good agreement (Fig.3) with the double-polarized G_E^p/G_M^p data although the newest data suggests a slower drop with Q^2 . The G_E^n/G_M^n calculation seems to rise rather faster with Q^2 than the data, although the slope suggested by the data is not entirely unambiguous.

0.1.1.4 Lattice QCD

A true *ab initio* approach to calculate the properties of hadrons is based on discretizing space-time into a four-dimensional lattice with a fixed lattice spacing and volume.

There have been several on-going calculations of form factors (e.g. [32]) using Lattice QCD (LQCD) but typically they have been limited to $Q^2 \lesssim 2.5$ (GeV/c)² due to worsening computational signal-to-noise ratio. Fig. 4 displays recent calculations [33] of neutron Dirac and Pauli form factors, which extend out to $Q^2 \lesssim 6$ (GeV/c)² (in the case of the quenched approximation) and compares them with a fit to the experimental neutron form factor data [20].

Differences in F_1 between quenched and dynamical studies indicate systematic error due to quenching, while F_2 appears less sensitive to sea-fermion effects. Due to the omission of “disconnected” diagrams F_1^n and G_E^n have relatively large systematic errors at moderate momentum transfer and accurate G_E^n data in the few-(GeV/c)² domain is certainly required to guide the LQCD effort. Presently a major impediment to reaching higher Q^2 is the granularity of the available lattices, but this situation will certainly improve.

The interplay between LQCD calculations, other calculational techniques and experiment can be very powerful. While LQCD calculations of form factors clearly have a way to go, they are already providing serious predictions that are

in reasonable agreement with experiment. They can also, for instance, be compared with non-lattice calculations in which the physical content of the theory is more readily evident. When lattice calculations, non-lattice calculations, and experiment are all found to agree, considerable insight can be gained.

0.1.1.5 Generalized Parton Distributions

Generalized Parton Distributions (GPD) [34, 35] describe correlations between spatial and momentum degrees of freedom and permit the construction of various types of "3-D images" of the nucleon. An example of a particularly powerful result to come out of GPDs is the "Ji Sum Rule" which relates the total angular momentum of the quarks to sums over some of the GPDs. The Ji Sum Rule provides an important key to understanding the origin of the spin of the nucleon.

Knowledge of the nucleon elastic form factors is critical to the experimental determination of GPDs since their first moments are related to the elastic form factors through model independent sum rules:

$$\int_{-1}^{+1} dx H^q(x, \xi, Q^2) = F_1^q(Q^2) \quad \int_{-1}^{+1} dx E^q(x, \xi, Q^2) = F_2^q(Q^2) \quad (2)$$

These relations are currently some of the most important constraints on the forms of the GPD's and, since it is extremely unlikely that the GPDs will be mapped out exhaustively in the near future, constraints such as those in Eq.2 will be critical to their practical determination. Already the constraints from Eq.2 have played an important role in the first estimates of nucleon quark angular momentum using the Ji Sum Rule and constraining GPDs is in itself an excellent reason to experimentally determine the nucleon elastic form factors.

A GPD based derivation of G_E^n/G_M^n is compared to the data in Fig.3. It is apparently consistent with the data, although the data are somewhat ambiguous around 1.5 (GeV/c)^2

0.1.1.6 Quark Orbital Angular Momentum

A common thread in virtually all of the theoretical explanations of the Q^2 -dependence of G_E^p/G_M^p is the role of quark orbital angular momentum (qOAM) in the internal dynamics. Evidence for qOAM also comes from other sources.

The DIS spin asymmetry A_1^n for the neutron [36] has been measured at high values of Bjorken x and compared with both relativistic CQM and pQCD predictions. The measured value of A_1^n was in disagreement with the pQCD prediction, which assumed hadron helicity conservation, but in reasonable agreement with the CQM calculations where qOAM has dynamical importance.

Single-spin (target) asymmetries in Semi Inclusive DIS (SIDIS) have been measured at HERMES [37], COMPASS [38] and recently at JLab [39, 40]. The interpretation of these asymmetries in terms of the Sivers mechanism is helping to illuminate the dynamical role for qOAM. From SPIN RHIC [41] the contribution of gluon spin ΔG to the nucleon spin is small, although the constraints on ΔG are not particularly stringent. The main message coming from all of this

work is that we have a poor understanding of the spin of the nucleon. Polarized DIS results suggest that only 20-30% of the composite spin is due to the spin of the quarks and it is certainly possible that some of the remaining spin is due to qOAM. As such, polarized SIDIS measurements will continue to be an important part of the Hall-A experimental programme post upgrade.

0.1.1.7 The Form Factors as a Hadronic Model Testing Ground

Fig.3, shows existing data for G_E^p/G_M^p and G_E^n/G_M^n , the projected errors for approved new experiments, and the results of several theoretical calculations, outlined in the previous subsection. The approved experiments associated with the SBS experiment are E12-07-109 (also known as GEp(5)), and E12-09-016 (also known as GEn(2)), which will measure G_E^p/G_M^p and G_E^n/G_M^n respectively. Fig.3, makes it clear that the only way to achieve clarity in discriminating between theoretical explanations of the G_E^p/G_M^p data is to measure the form factors with high precision to high values of Q^2 for both the proton and the neutron. For example three of the predictions shown, the relativistic constituent quark model [31, 26], the DSE/Faddeev calculation [22] and the refined pQCD calculation [18], all show G_E^p/G_M^p crossing zero somewhere in the neighborhood of 10 (GeV/c)². In contrast, the two Vector Meson Dominance (VMD) models show G_E^p/G_M^p approaching zero much more gradually [23, 24, 25].

Looking at the neutron, even by ~ 4 (GeV/c)² the RCQM, pQCD and DSE/Faddeev calculations all differ markedly from one another. In the years following the discovery of [10] it is not surprising that models have evolved to explain the existing proton data. It is also not surprising that these models diverge strongly where there is little or no data to constrain the calculations. This applies at higher Q^2 for the proton and down to moderate Q^2 for the neutron. In general, higher values of Q^2 also offer some theoretical simplifications that are not valid in a softer regime. For instance, the role of vector mesons is suppressed at higher Q^2 , as are higher Fock states in some of the phenomenological models, so that there are generally fewer places to hide deficiencies in a model.

The data for G_E^p/G_M^p are linear up to ~ 6 (GeV/c)², but the results from GEp(3) [14], up to values ~ 8.6 (GeV/c)², suggest a flattening of the gradient of G_E^p/G_M^p . By going to 14.5 (GeV/c)² the trend of G_E^p/G_M^p should become clear, but only if the data have sufficient precision. The projected errors for GEp(5), which is based on SBS, present a challenge to theory out to 14.5 (GeV/c)², since the SBS approach provides a factor of 10 improvement in the polarimeter Figure-of-Merit. Eventually (from pQCD) G_E^p/G_M^p should level off and become constant. Evidence of a transition to this behavior would provide valuable insight and it is important to have an experiments capable of achieving high precision at high Q^2 .

With respect to the neutron, the measurement of G_E^n/G_M^n out to $Q^2 = 10$ (GeV/c)² has tremendous potential to assess various nucleon structure models. However the various predictions for the neutron all start to diverge strongly above 3 (GeV/c)² and further high-precision measurements in this region, using a different experimental technique, are required to confirm the GEn(1) results [8] and the previous Hall-C recoil polarimetry results [9]. Where the two data sets meet around 1.5 (GeV/c)² there is an interesting possible discrepancy, although the statistical significance is marginal. This emphasises the need for high-precision,

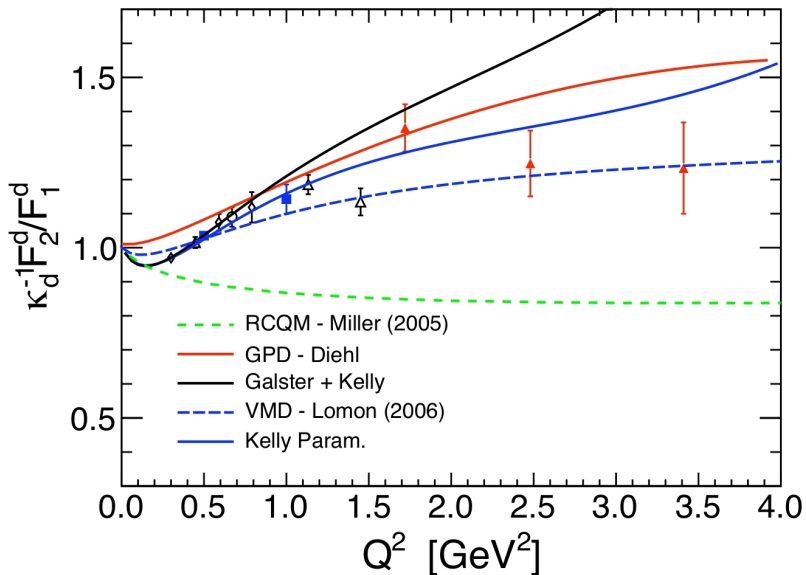


Figure 5: Q^2 dependence of separated d quark ratio $\kappa_d^{-1} F_2^d / F_1^d$.

accurate neutron data in providing unambiguous guidance to theory. Measurement to high Q^2 is vital, but it is no less important to have top-quality data at moderate Q^2 . Theoretical divergence is less pronounced in this region, but it is possible to achieve much better precision at moderate Q^2 and achieve low systematic uncertainties in a ${}^2\text{H}(\bar{e}, e' \bar{n})$ measurement. Moderate Q^2 is also optimum to illuminate longer-range structure effects.

Fig.5 displays the separated d quark ratio F_2^d / F_1^d which requires both proton and neutron data. It is evident that the current level of experimental precision needs to be improved to provide unambiguous theoretical guidance.

0.2 Observables and Previous Experiments to Access the Form Factors

The present experiment will be part of a programme in Hall-A to measure the 4 nucleon Sachs form factors to multi- $(\text{GeV}/c)^2$ values of Q^2 . With sufficient precision and accuracy, these will provide a severe challenge to existing, QCD-inspired models of the nucleon and eventually to LQCD calculations.

The most general form for a relativistically covariant hadronic current for a spin-1/2 nucleon which satisfies current conservation is

$$J_{hadronic}^\mu = e\bar{N}(p') \left[\gamma^\mu F_1(Q^2) + \frac{i\sigma^{\mu\nu}q_\nu}{2M} F_2(Q^2) \right] \quad (3)$$

where $\bar{N}(p')$ is the nucleon Dirac spinor for the final momentum p' , and $F_1(Q^2)$

and $F_2(Q^2)$ are the Dirac (helicity conserving) and Pauli (helicity flip) form factors. It is often convenient to express cross sections and other measurable quantities in terms of the Sachs electric and magnetic form factors which are linear combinations of F_1 and F_2 .

$$G_E = F_1 - \tau F_2 \quad G_M = F_1 + F_2 \quad (4)$$

where $\tau = Q^2/4M_N^2$. A brief review of experimental techniques to access the form factors is presented below.

0.2.1 Rosenbluth Separation

The electric (G_E) and magnetic (G_M) form factors represent, in the Breit frame, the Fourier transforms of the distributions of charge and magnetic moment respectively of the nucleon constituents. As measured in elastic electron scattering, they are functions of Q^2 , the squared four-momentum transfer, and may be extracted from the differential cross section, which can be cast in the form:

$$\sigma(\theta) = \sigma_M(\theta) \left\{ \left[\frac{G_E^2(Q^2) + \tau G_M^2(Q^2)}{1 + \tau} \right] + 2\tau G_M^2(Q^2) \tan^2 \frac{\theta_e}{2} \right\} \quad (5)$$

$$\sigma_M = \frac{\alpha^2 \cos \frac{\theta_e}{2}}{4E_e^2 \sin^4 \frac{\theta_e}{2}} \cdot \frac{E'_e}{E_e}$$

where σ_M is the Mott cross section (with recoil correction) for scattering from a point object, θ_e is the electron scattering angle and $\tau = Q^2/4M_N$. The Rosenbluth technique to separate electric and magnetic components entails measurement at different combinations of electron beam energies and scattering angle, such that Q^2 is held constant. After Hofstadter performed pioneering measurements in the 1950's [1], the precision improved and kinematic range extended. In the case of the proton, for relatively low momentum transfer, Rosenbluth separation seems to work reasonably well. However for G_E^n and G_E^p at high Q^2 , where $G_E \ll G_M$, it is extremely difficult to determine G_E with any reasonable degree of precision or accuracy. Rosenbluth is a demanding technique requiring extreme care in accounting for changes in detector acceptance, among other things.

Another more subtle issue has emerged in recent years. The validity of Eq.5 depends on the one-photon-exchange or Born approximation. It has now been established that two-photon contributions to the cross section at higher values of Q^2 are sufficiently large that the separation of the form factors has been severely compromised. This makes the determination of electric form factors by alternative techniques vital. The difference between G_E^p/G_M^p measurements taken using a double-polarized technique or Rosenbluth separation is illustrated in Fig.0.1.1.1.

0.2.2 Double polarized measurements

The double polarization method for the measurement of the G_E was originally proposed [42] to improve the experimental sensitivity to the spin-flip form factor

F_2 at large momentum transfer, and subsequent work [43] developed the formalism. However the experimental realization of these techniques had to wait for high-intensity, high-duty-factor accelerators, capable of delivering polarized electron beams. A number of form-factor measurements have been performed in recent years, using two versions of the double-polarization method: either with polarized nucleon targets, or with a polarimeter to measure the polarization transfer to the recoiling nucleon. The technique of choice depends on the comparison of achievable luminosity, detector efficiency, detector acceptance and the experimental asymmetry, which in turn depends on the target polarization or polarimeter analysing power. In the case of the neutron there is no free target and quasi-elastic scattering from the neutron embedded in ^2H or ^3He offers the nearest practical approximation to the free case. Bound-nucleon and final-state-interaction effects have to be accounted for and comparison of data from different targets is a vital check on the corrections. Neutron measurements are inherently more challenging than their proton equivalents, as demonstrated by their more restricted kinematic range $G_E^n/G_M^n : Q^2 \leq 3.5 \text{ (GeV/c)}^2$ as opposed to $G_E^p/G_M^p : Q \leq 8.5 \text{ (GeV/c)}^2$. Even at $Q^2 \sim 4 \text{ (GeV/c)}^2$ a precise value of G_E^n/G_M^n has extremely high selectivity of the quite diverse predictions of various theoretical models, but it is vital to have reliable, independently verified neutron results.

Whether working with a polarized target or a recoil polarimeter, the ability separate G_E from the much larger G_M and the relative freedom from two-photon exchange effects make double-polarization asymmetry measurements the techniques of choice for measuring G_E^n .

0.2.2.1 Polarized Beam and Polarized Target

The asymmetry may be expressed as

$$A = A_{\perp} \sin \theta \cos \phi + A_{\parallel} \cos \theta = \frac{a G_E/G_M \sin \theta \cos \phi}{(G_E/G_M)^2 + c} + \frac{b \cos \theta}{(G_E/G_M)^2 + c} \quad (6)$$

where $a = -2\sqrt{\tau(1+\tau)} \tan(\theta_e/2)$, $b = 2\sqrt{\tau [1 + (1+\tau) \tan^2(\theta_e/2)]}$,

$c = \tau [1 + 2(1+\tau) \sin^2(\theta_e/2)]$, ϕ' is the angle between the nucleon and electron scattering planes and θ' is the angle the the nucleon polarization makes with \vec{q} . Where $\phi' \sim 0,180$ and $\theta' \sim 90$, $A \propto G_E/G_M$.

The projected errors for the new GEN(2) experiment (Fig.3) are roughly 20% for data points on the often cited Galster parameterization. The three GEN(1) data points, currently the highest-value Q^2 points in existence, have uncertainties $\sim 15\%$. While it is clear that, in terms of precision, polarized target experiments are better at $Q^2 \sim 10 \text{ (GeV/c)}^2$, we are confident that recoil polarimetry is highly competitive at $Q^2 \lesssim 4 \text{ (GeV/c)}^2$.

0.2.2.2 Polarized Beam and Recoil Polarimetry

In the case of a free nucleon the polarization transferred from the electron to the nucleon can be written as:

$$P_x = -hP_e \frac{2\sqrt{\tau(1+\tau)} \tan \frac{\theta_e}{2} G_E G_M}{G_E^2 + \tau G_M^2 (1 + 2(1+\tau) \tan^2 \frac{\theta_e}{2})} \quad (7)$$

$$P_y = 0 \quad (8)$$

$$P_z = hP_e \frac{2\tau \sqrt{1+\tau + (1+\tau)^2 \tan^2 \frac{\theta_e}{2}} \tan \frac{\theta_e}{2} G_M^2}{G_E^2 + \tau G_M^2 (1 + 2(1+\tau) \tan^2 \frac{\theta_e}{2})} \quad (9)$$

$$\frac{P_x}{P_z} = \frac{1}{\sqrt{\tau + \tau(1+\tau) \tan^2 \frac{\theta_e}{2}}} \cdot \frac{G_E}{G_M} \quad (10)$$

where h and P_e are the helicity and polarization respectively of the electron beam. Thus the ratio $P_x/P_z \propto G_E/G_m$ and G_M may be obtained from the differential cross section (Eq.5). In the case of the neutron, a free-nucleon target is not feasible and here one must use quasi-elastic scattering from the neutron embedded in a nucleus. The deuteron is an obvious choice as the $p-n$ system is bound weakly, so that quasi-free scattering is a reasonable approximation to the free case at incident momenta greater than ~ 1 GeV. In addition, the handling of interactions of the $p-n$ final state is considerably simpler than in the case of $p-p-n$ from a ${}^3\text{He}$ target.

Eq.10 requires the measurement of the longitudinal component of the neutron polarization and this must be precessed into the transverse plane. The angle of precession through a magnetic field may be expressed as

$$\chi = \frac{2\mu_n}{\hbar c} \frac{1}{\beta_n} \int_L \mathbf{B} \cdot d\mathbf{l} \quad (11)$$

where $L(x, y, z)$ is the path through the field, $\mathbf{B} = (B_x, B_y, B_z)$ is the flux density, μ_n is the neutron magnetic moment and β_n is the neutron velocity. With a horizontal field $(B_x, 0, 0)$ the spin will precess in the $y-z$ plane (See Sec.0.2.3).

0.2.3 Nucleon Polarimetry

Nucleon polarimetry depends on the spin-orbit interaction of an incident nucleon with a target nucleon or nucleus, which produces an azimuthal modulation of the scattering process:

$$\sigma(\theta'_n, \phi'_n) = \sigma(\theta'_n) \left[1 + A_y^{eff}(\theta'_n) \left\{ P_x^n \sin \phi'_n + P_y^n \cos \phi'_n \right\} \right] \quad (12)$$

where $\sigma(\theta'_n)$ is the unpolarized differential cross section, $A_y^{eff}(\theta'_n)$ is the effective analyzing power of the scattering process and P_x^n, P_y^n are respectively the horizontal and vertical components of the incident nucleon polarization. Scattering angles are defined in Fig.6. Note that there is no dependence on the longitudinal component P_z^n . A schematic representation of a typical polarimeter geometry is given in Fig.6. The effectiveness of any polarimeter will depend on its detection efficiency and the analyzing power, which can be parametrized as a figure of merit \mathcal{F} given by:

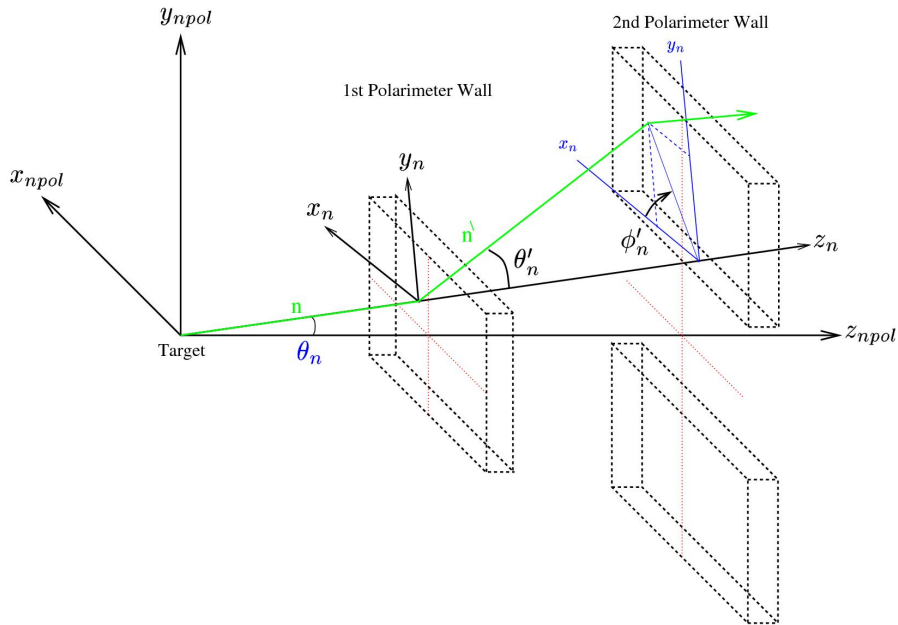


Figure 6: Schematic view of a typical neutron polarimeter. In this proposal incident neutrons would be directed along axis z_{npol} .

$$\mathcal{F}^2(p_n) = \int \varepsilon(p_n, \theta'_n) A_y^2(p_n, \theta'_n) d\theta_n \quad (13)$$

where $\varepsilon(p_n, \theta'_n)$ is the detection efficiency which depends on the cross section for the scattering process, the thickness of the polarimeter material and the useful angular range covered. Obviously one would restrict the angular range to that where A_y is large. The thickness is usually limited in practice by multiple scattering considerations. If \mathcal{F} is known then the precision of the obtained incident polarization may be estimated as:

$$\Delta P = \sqrt{\frac{2}{N_{inc} \mathcal{F}^2}} \quad (14)$$

where N_{inc} is the number of incident particles. Note that the split rear wall depicted in Fig.6 is not a general polarimeter feature. If one wishes to untangle P_x and P_y polarization components and maximize acceptance then full azimuthal coverage is preferable. In the present project the rear detector will be a segmented hadron calorimeter similar to that designed in Dubna [44] for the COMPASS experiment at CERN. With this detector we will have full azimuthal coverage up to polar angles of $\sim 10^\circ$, which will contain most of the forward peaked scattering. Thresholds can be set high to suppress soft background so that the device can operate comfortably while open to the target.

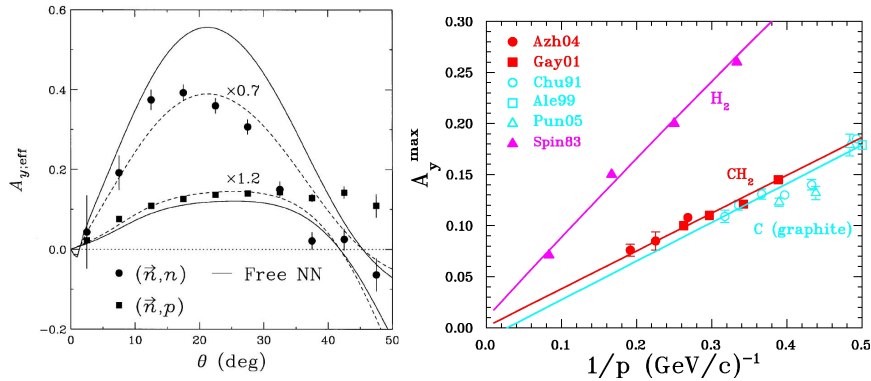


Figure 7: Nucleon scattering analyzing powers. Left neutron measurements from [51]. Right proton measurements from [50, 6, 49].

0.2.3.1 Neutron Analysing Power at Several GeV/c

In comparison to the proton, neutron scattering analysing powers are rather poorly known. Elastic n-p scattering has been measured up to 6 GeV [45] and both this and p-p has been parametrised [46]. Quasi-elastic p-n scattering has also been measured at SATURNE [47] up to around 2.4 GeV and this data has been included in the SAID partial wave analysis [48] of nucleon-nucleon scattering data. SAID has no information on quasi-free n-n scattering and the fits to n-p are unlikely to be reliable in the several-GeV domain.

For protons free p-p scattering [49] has a factor ~ 2 greater analysing power than scattering from ^{12}C or CH_2 , as shown in Fig.7 which demonstrates the highly linear behaviour [50] of the maximum analysing power A_y^{max} (dependent on scattering angle) as a function of $1/p_p$. Ref. [50] has parametrised measurements of the p-p analysing power of CH_2 at several GeV and these data have been used in the design of the G_E^p/G_M^p experiments at JLab. A useful ‘‘rule of thumb’’ to emerge from this work is that A_y^{max} occurs at $P_{\perp} = p_p \sin \theta_p \sim 0.3 \text{ GeV}/c$

Measurements of quasi-free n-n and n-p scattering from plastic scintillator have been made at $p_n = 632 \text{ GeV}/c$ [51] and the main results are plotted in Fig.7. The angular distributions are not inconsistent with the idea that A_y^{max} occurs at $P_{\perp} = p_n \sin \theta_n \sim 0.3 \text{ GeV}/c$.

It is clear that neutron analysing powers are poorly known at momenta of several GeV/c and that a quantitative estimate of the beam time required to achieve a given precision in neutron recoil polarimetry needs data. The means to achieve this is discussed in Sec.0.3.4.

0.2.4 Previous Form Factor Measurements and Proposals

0.2.4.1 Unpolarized

Recently a new Rosenbluth measurement of the proton form factors [17] at Q^2 values of 2.64, 3.20 and 4.10 $(\text{GeV}/c)^2$ has been made in Hall-A. Differential cross sections were determined by detecting the recoiling proton, in contrast to

previous measurements where the scattered electron was detected, and relative cross sections were claimed to better than 1%. The measurement focussed on the extraction of G_E^p/G_M^p which was determined to 4-8% and found to follow form factor scaling, i.e. $\mu G_E \sim G_M$. These results (Fig.2) are consistent with, and much more precise than, previous Rosenbluth extractions. They are in definite disagreement with recent polarization transfer measurements of comparable precision, which may be attributed to the relative sensitivity of Rosenbluth separation to two-photon-exchange effects.

0.2.4.2 Polarized Target

Vector Polarized ^2H has the neutron and proton spins aligned in parallel and measurements with such a polarized neutron-proton target have been made at $Q^2 = 0.21$ [52] and 0.495 (GeV/c^2) [53]. Corrections for various effects amounted to $\sim 13\%$ in [53], compared to $\sim 8\%$ for a recoil polarimetry experiment [54] at slightly lower Q^2 .

Polarized ^3He has the advantage that $\sim 90\%$ of the nuclear polarization is carried by the neutron. At Mainz, polarized ^3He target measurements have taken place at $Q^2 = 0.385$ (GeV/c^2) [55] and 0.385 (GeV/c^2) [56], Subsequent measurements at 1.5 (GeV/c^2) are not yet finalised. In the GEN(1) experiment at JLab [8] the high beam energy, high performance ^3He target and large acceptance detectors has enabled the Q^2 range to be stretched up to 3.4 (GeV/c^2).

The effective figure of merit of GEN(1) represents more than an order-of-magnitude increase over previous experiments to measure G_E^n/G_M^n and already the results are providing valuable insight regarding the scaling of the form factors. In Ref.[18] the proton results were explained quite well by a logarithmic scaling brought about by the introduction of non-zero quark orbital angular momentum. Application of this scaling to the neutron data is shown in the bottom plot of Fig.3 as a black dot-dash line, and it is clearly well above the data points from GEN(1). The prediction of the "light front cloudy bag model" of Miller [26], which anticipated the scaling results of G_E^p/G_M^p , also appears to overestimate the slope of G_E^n/G_M^n with Q^2 . It is clear is that much can be learned by extending neutron measurements to yet higher values of Q^2 and Hall-A experiment E12-09-016 [4], which will extend to 10 (GeV/c^2), has been awarded 50 days of beam time.

0.2.4.3 Recoil Polarimetry

There have been several experiments to measure G_E^n/G_M^n by recoil polarimetry. Proof-of-principle measurements at MIT-Bates [57] were followed by more quantitative measurements at Mainz, firstly within collaboration A3 [54, 58] and subsequently within collaboration A1 [59]. While the Mainz programme was still in progress, experiments at JLab started to come online, and Hall-C measurements of G_E^n/G_M^n have been published at Q^2 of 0.5 and 1.0 (GeV/c^2) [60] and 1.45 (GeV/c^2) [9]. The beam energy at JLab is significantly higher than Mainz (currently 6.0 GeV, as opposed to 1.6 GeV and in 2013 a high intensity 11 GeV beam will become available at JLab. The higher beam energy is obviously important to achieve the high Q^2 G_E^p/G_M^p data points of GEp(5), but

for G_E^n/G_M^n measurements at somewhat lower Q^2 , a lower beam energy gives superior kinematic conditions.

At JLab, experiment PR-09-006 using the ${}^2\text{H}(\vec{e}, e'\vec{n})$ reaction has been proposed [61] for Hall-C up to $Q^2 = 7$ (GeV/c) 2 , although beam time has not yet been awarded. The practice and interpretation of all G_E^n/G_M^n measurements is very challenging and independent verification of data should be mandatory. Thus we believe that a new ${}^2\text{H}(\vec{e}, e'\vec{n})$ experiment is necessary and timely. In our opinion the present proposal has several advantages over PR-09-006 which are discussed in Sec.0.2.5.1.

The G_E^n/G_M^n measurement by recoil polarimetry would be a component of the Hall-A programme to measure all 4 nucleon form factors to high precision, over a broad range of Q^2 . The equivalent measurements of G_E^p/G_M^p by recoil polarimetry [6] rely heavily on proton analysing power measurements at Dubna [62] to quantify the figure of merit of the polarimeter (Eq.13). We plan an analogous neutron measurement [63] to support the present and possibly future proposals.

0.2.5 New Elastic Form Factor Measurements at JLab.

Measurement of the nucleon elastic form factors will be a major theme in Hall-A with the upgraded CEBAF accelerator. The SBS project has three approved measurements: one on G_E^p/G_M^p [6], one on G_E^n/G_M^n [4], and on G_M^n/G_M^p [5] by the cross section ratio method. These three measurements, together with a very precise measurement of G_M^p [7] in Hall A using the HRS Spectrometers (not part of the SBS Program), will collectively determine all four nucleon form factors with unprecedented reach in Q^2 and accuracy. The figures of merit provided by the various SBS configurations represent an improvement of between 10 and 50 over all past and proposed experiments. Thus the achievable precision made possible by the SBS apparatus is second to none, and will provide a challenge to theory for many years to come. We briefly describe our experimental plan for each of the three proposed measurements.

1. G_E^p/G_M^p up to 14.5 (GeV/c) 2 using Recoil Polarization.

Experiment E12-07-109 or GEp(5), will measure the ratio G_E^p/G_M^p at $Q^2 = 5, 10, 14.5$ (GeV/c) 2 , close to doubling the maximum Q^2 -value of GEp(3) while maintaining a relative uncertainty of ~ 0.1 (Fig.3). The GEp(5) experiment will use the 11 GeV polarized electron beam, a 40 cm long liquid hydrogen target, and a customised detector system. An electromagnetic calorimeter, "BigCal", will detect the elastically scattered electrons. SBS, equipped with a double polarimeter, will be used for the detection of the recoiling proton.

2. Precision Measurement of the Neutron Magnetic Form Factor up to $Q^2 = 13.5$ (GeV/c) 2 .

The combination of precision measurements of G_M^p and G_M^n will permit the reconstruction of the individual u and d quark distributions with an impact-parameter resolution of 0.05 fm. These data are needed both to determine the $u - d$ difference and to study the QCD mechanisms which govern these distributions. Eventually it is hoped to reach as high as

$Q^2 \leq 18$ (GeV/c)² in Hall-A [5], which will match the kinematic reach of the G_M^p experiment [7]. The magnetic form factor of the neutron has been measured accurately up to 4.5 (GeV/c)² [64], but the existing data for higher Q^2 [65] have uncertainties of about 10-20%. In E09-019 [5] G_M^n will be obtained from the cross-section ratio of ${}^2\text{H}(e, e'n)$ and ${}^2\text{H}(e, e'p)$ quasi-free scattering from the deuteron. This ratio method has also been proposed using CLAS12 [66], which can measure on a fine grid of Q^2 points. However the SBS measurement can be made at much higher luminosity and can achieve superior precision at high Q^2 . The HCAL calorimeter for the SBS measurement offers very similar proton and neutron detection efficiencies which are close to 100%. This largely eliminates a potential major source of systematic uncertainty in the ratio method.

3. G_E^n/G_M^n up to $Q^2 = 10$ (GeV/c)². Experiment E12-09-016 [4] (GEn(2)), will measure the double-spin asymmetry in quasi-elastic ${}^3\text{He}(\vec{e}, e'n)\text{pp}$ using a new highly-polarized ${}^3\text{He}$ target, capable of withstanding beam currents as high as 65 μA . The scattered electron will be detected in BigBite which was also used successfully during GEn(1). The BigBite detector stack will be upgraded to include a GEM tracking system and the recoiling neutron will be detected using a large segmented hadron calorimeter HCAL. HCAL will also be used in E12-07-109 and E12-09-019. For E12-09-016 the SBS dipole magnet will be located between the target and the neutron detector, to facilitate the separation of charged and neutral quasi-elastic events. The physics impact of GEn(2) is illustrated in Fig.3, which shows both existing and projected data. Measurements are proposed at $Q^2 = 1.5, 3.7, 6.8, 10.2$ (GeV/c)² which can be compared to the current highest GEn(1) point at $Q^2 = 3.4$ (GeV/c)². However, given that neutron measurements are extremely challenging, it is vital to have independent confirmation of the polarized target results. There is a hint (Fig.3: bottom plot) that recoil-polarimetry and polarized-target G_E^n/G_M^n measurements may not be entirely consistent at $Q^2 \sim 1.5$ (GeV/c)². The present proposal to measure the range 1.5 – 4.0 (GeV/c)² to high accuracy and precision has the potential to settle any possible ambiguities in the current data set.

0.2.5.1 Comparison of the Present Proposal to Hall-C Proposal PR-09-006

A measurement of G_E^n/G_M^n by recoil polarimetry has been proposed [61] for Hall-C using the Super High Momentum Spectrometer (SHMS) and a custom built polarimeter. We believe that the apparatus described in this proposal offers many advantages:

- Compared to the SHMS, BigBite offers greatly increased angular acceptance on the electron and hadron arms. BigBite and the neutron-arm acceptance are well matched. The large acceptance is vital to achieve good counting statistics in a reasonable time.
- The present polarimeter will have superior detection efficiency to the Hall-C polarimeter through use of a high efficiency analyzer and a hadron

calorimeter (HCAL) to detect the neutron-scattering azimuthal distribution.

- At large neutron momentum the scattering angles in the polarimeter for optimum analysing power are small so that the polarimeter needs to have full forward angle coverage. HCAL has almost full azimuthal coverage up to $\theta'_n \sim 10^\circ$ and also has good position resolution. It can function comfortably in full view of the target as background can be suppressed very effectively without losing much efficiency.
- The elements of the neutron-scattering analyser array are aligned with their long axes parallel to the incident particles. This provides good angular resolution and each element presents a smaller area to the target. The timing resolution remains good for the parallel aligned bars and the array covers the full angle range defined by the SBS dipole aperture. Present estimates indicate that the analyzer will function effectively with relatively minimal lead shielding up to 50 mm thick. In PR-09-006 the proposed polarimeter shielding is 150 mm.
- The present proposal is made in conjunction with a proposal to measure neutron analyzing powers at the Nuclotron accelerator in Dubna. This measurement is an integral part of the present project which will remove much of the uncertainty in estimating figures of merit for neutron polarimetry.
- In the present proposal neutron spin components P_x and P_z are determined simultaneously at a single magnitude of the neutron spin precession field. In PR-09-006, which uses a vertical (as opposed to the present horizontal) field direction, P_z is rotated by varying amounts into the x direction by varying the magnetic field. This will change the background levels in the polarimeter and hence the potential systematics of the asymmetry due to changes of the running conditions.
- In PR-09-006 P_z is mixed with P_x by variable amounts, by varying the field and hence the precession angle. This angle must be known to high accuracy to avoid significant systematic distortions, which may be difficult in practise at an integrated field strength of ~ 4.5 Tm where the dipole field will be highly saturated. Mixing of P_x and P_z will also occur in the present apparatus (Sec.0.3.2.4), but in this case due to fringe fields and different paths through the the dipole. Assuming that the field characteristics are well determined this can in principle be corrected with good accuracy.
- The present experiment will use 50 mm of Pb shielding before the polarimeter, as opposed to 150 mm employed in PR-09-006, so that $p - n$ interactions in the Pb will present less of a potential source of asymmetry dilution. The use of different targets (^1H , ^3He and ^{12}C in addition to ^2H) in the present experiment will provide different relative incident proton fluxes to facilitate evaluation of this effect.

Other aspects of the present apparatus, while not superior to PR-09-006, are more than adequate for the present experiment and present no significant compromising of performance.

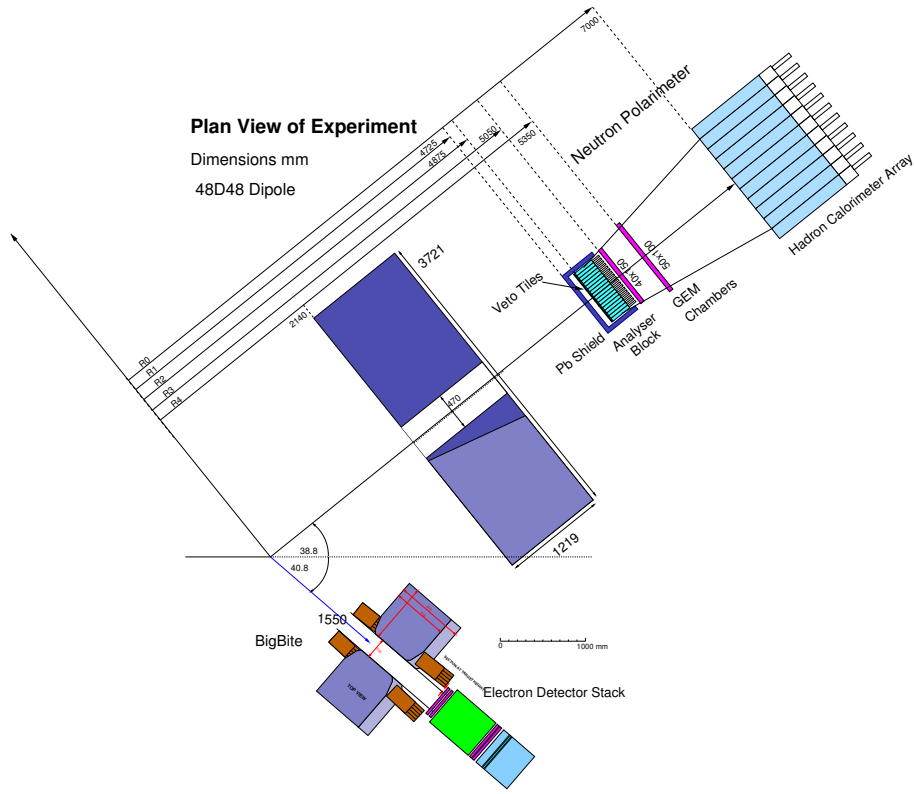


Figure 8: Plan view of experiment $Q^2 = 1.5 \text{ (GeV/c)}^2$

- BigBite, with a $\sim 1 \text{ mr}$ angular resolution and a momentum resolution of $\sim 0.5\%$, is well suited to the quasi-elastic scattering process, where little is gained by having very high resolution. The GEM high-resolution tracking system will remove limitations on BigBite luminosity, imposed by the previous MWDC trackers.
- The SBS dipole, with a maximum integrated field strength of $\sim 2 \text{ Tm}$ induces a spin precession angle $\chi > 70^\circ$, so that after precession $P_y \gtrsim 0.94P_z$, where P_z is the original longitudinal component. The magnetic field also gives very clean separation of neutrons and protons and sweeps all particles of momentum $< 750 \text{ GeV/c}$ out of the polarimeter acceptance.

Detail of the present apparatus can be found in Sec.0.3.

0.3 Experimental Method

The polarization transfer method requires a large number of counts because of the relatively low analyzing power of the polarimeter. Going to high momentum transfer, where the effective elastic scattering rate scales approximately as E_{beam}^2/Q^{16} , requires high luminosity, large acceptance and a high rate capability

in the detection system. A plan view of the detector apparatus is displayed in Fig.8.

We propose to perform the measurement in Hall-A of Jefferson Laboratory, using the CW, polarized electron beam from the CEBAF accelerator. This will have a maximum energy of 11 GeV and maximum current of 80 μ A. The present experiment will not require 11 GeV and we have chosen the beam energies (Table 1) to be at integral factors of a 1.1 GeV energy gain per pass (1/2 of the maximum 2.2 GeV available) through the accelerator. Beam polarizations in excess of 80% have been achieved routinely during 6 GeV operation of CEBAF and 80% is assumed for estimates of precision in measuring form factor ratios.

The electrons will be incident on a 10 cm long liquid deuterium (LD₂) target with 100 μ m Al entrance and exit windows, giving ~ 0.054 g/cm² of material, compared to ~ 1.69 g/cm² for the LD₂. A liquid hydrogen (LH₂) target will also be used for calibrations. A 40 μ A electron beam incident on a 10 cm LD₂ target produces a neutron luminosity of $\sim 1.26 \times 10^{38}$ cm⁻²s⁻¹.

Scattered electrons are detected in the BigBite spectrometer, which will reconstruct the momentum, direction and reaction vertex. The neutron arm will be a polarimeter which consists of a plastic scintillator analyser block, equipped with charged-particle veto tiles, followed by GEM trackers and the hadron calorimeter HCAL. The polarimeter will provide position and time-of-flight information on the recoiling nucleon as well as scattering asymmetries. Neutron spin precession will be performed by the "48D48" dipole which is the basis of the SBS charged-particle spectrometer. The experimental components are described in more detail in the following subsections.

0.3.1 The e' Detector BigBite

BigBite (Fig.9) is a large-acceptance, non-focusing magnetic spectrometer which, when positioned with the entrance aperture of the dipole 1.55 m from the target center, subtends a solid angle of ~ 75 msr. Fig. 9 shows BigBite equipped with lead glass pre-shower and shower counters to provide a trigger which is insensitive to low energy background. In conjunction with a gas Cherenkov, these counters distinguish electrons cleanly from π^- . Tracking is performed by two 400 \times 1500 mm Gas Electron Multiplier (GEM) chambers at the front, followed, after a flight path of ~ 650 mm, by a two 500 \times 2000 mm GEM chambers. The GEM trackers supercede the MWDC, used in pre-upgrade experiments, and offer increased counting rate capability so that higher luminosities may be achieved. At CERN they have proved capable [67] of operating at incident fluxes of 2.5 MHz/cm². They will be assembled from the 400 \times 500 mm modules which are being constructed for the SBS programme of experiments. The GEM will have a position resolution $\sigma_r \sim 70$ μ m (60 μ m has been obtained from prototype tests) and the two groups of trackers are separated by around 0.65_m. The angular resolution may estimated from

$$\delta\theta = \sqrt{\left(\frac{\sigma_r}{z_{tr}}\right)^2 + \left(\frac{13.6}{\beta c p_e} \sqrt{\frac{x}{X_0}} \left[1 + 0.038 \ln\left(\frac{x}{X_0}\right)\right]\right)^2} \quad (15)$$

where p_e is the electron momentum in MeV/c and x/X_0 is the thickness of intervening material in radiation lengths. This translates to an angular reso-

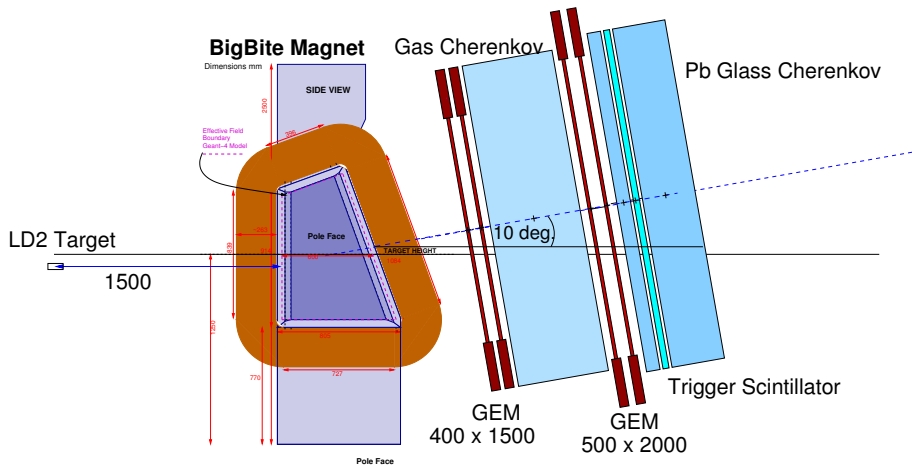


Figure 9: Side view of BigBite as configured for e' detection

lution of $\sigma \sim 1$ mr in both dispersive and non-dispersive directions. For the relatively small deflection obtained with an integrated field strength of 1.2 Tm and electrons of 1–2.5 GeV/c, the angle of deflection is given by:

$$p_e \approx \frac{e \int B \cdot dl}{\theta} \quad (16)$$

The momentum resolution of $\delta p/p \sim 0.5\%$ will be entirely adequate for the present experiment (Sec.0.4.3). The z-vertex resolution at the target is around 4 mm. It is extremely important to have an accurate knowledge of the vertex and four-momentum of the virtual photon. At each kinematic setting the BigBite optics and vertex reconstruction will be calibrated using a sieve slit and multi-carbon-foil target. Momentum will be calibrated using elastic ep scattering from a LH_2 target.

Timing from BigBite is provided by the array of trigger scintillators. For high luminosity operation a new, finer granularity, hodoscope will be provided. This will consist of 90 plastic scintillator elements, each $25 \times 25 \times 600$ mm. The intrinsic timing resolution of this device should be around 0.5 ns FWHM.

Offline charged particle identification is aided by the threshold gas Cherenkov. Light is collected by a combination of spherical, plane and conical mirrors and reflected on to a set of 20 PMT's. These are arranged symmetrically to the left and right of the central trajectory through the spectrometer.

The Pb-glass pre-shower - shower trigger detector is quite insensitive to charged pions but does not discriminate electrons from π^0 decay photons.

If it becomes necessary to reduce BigBite trigger rates, we plan to use a “pixel fast readout” GEM chamber where the readout board is arranged in 50×50 mm pads. It is possible to read a fast signal directly from each pad which has dimensions suitable for trigger coincidences with the Pb-glass counters. BigBite rates are discussed in Sec.0.4.2.

0.3.2 The Neutron Polarimeter

The neutron polarimeter (Fig. 8) consists of four main components:

1. An array of plastic scintillator blocks aligned with their long axes parallel to the direction of the recoiling neutrons. This acts as an active polarisation analyser through the azimuthal modulation of the neutron-nucleus scattering angle.
2. An array of plastic scintillator veto tiles, sited directly in front of the analyser provide charged particle identification.
3. A GEM based tracker for charged particles produced in the analyser before detection in HCAL. This will be built from the 40×50 cm GEM modules which are being constructed for the SBS project
4. A hadron calorimeter HCAL, which is optimised to detect nucleons with momenta of 1.5 - 10 GeV/c with high efficiency. This segmented calorimeter, together with the segmented analyser array (and the GEM tracker for charge-exchange scattering), determines the scattering angle of the neutron used to analyse the spin polarisation of the recoiling neutron.

A small-scale version of the device proposed here (Fig.14) is currently being assembled for neutron analysing power measurements at the Nuclotron accelerator at JINR in Dubna. This project is summarized in Sec.0.3.4.

0.3.2.1 The Plastic Scintillator Analyser Array and Veto Detector

The analyzer consists of a 18×48 array of $40 \times 40 \times 250$ mm bars of EJ-200 plastic scintillator [68], aligned with their long axes parallel to the incident neutrons. Each bar will be read out by a 28 mm ETL 9125 Photomultiplier (PMT) of the type used originally in the DIRC detector of BABAR [69]. The original voltage dividers, designed for a few-photon detection situation, are not suitable for the present analyser array and an alternative design suitable for high-rate scintillation counting will be implemented for the present experiment. PMT's are attached on the downstream side of the detector modules. Neutrons will interact all along the 25 cm length of the analyser bars giving an uncertainty in flight path and hence time of flight. This is partially compensated by the transit time of scintillation light ($\eta_{scint} \sim 1.5$, $\beta \sim 2/3$) to the PMT photo cathode, and taking both analyser length and target length into consideration the flight time uncertainty is ~ 0.4 ns for 1.5–3 GeV/c nucleons. The ETL 9125 has a linear focused dynode structure which minimises time uncertainties in the electron transport. If one estimates the intrinsic timing resolution of the PMT for scintillation counting to be ~ 0.75 ns FWHM (the resolution quoted in [69] is 3.5 ns FWHM for single-photon counting) then the overall timing resolution would be ~ 0.9 ns FWHM.

A finely segmented analyser is obviously desirable in terms of its position resolution (see Sec.0.4.1.1) and counting rate. The 40×40 mm cross section represents a reasonable compromise in terms of cost and compatibility with the available PMT's. A simulation of the effect of analyzer-bar size on resolution is presented in Sec.0.4.1.1. Counting rates in the analyser are discussed in Sec.0.4.2.

In front of the analyser array comes a set of $80 \times 80 \times 10$ mm tiles of plastic scintillator, each covering 2×2 analyser bars. These will aid the distinguishing of incident charged and neutron particles, especially in cases where incident particles interact with the Pb shield.

0.3.2.2 The GEM Charged Particle Tracker

The analyser is followed by a tracker of the charged particles produced by neutron charge-exchange or hadronic-shower processes within the analyser. This increases the information obtained on the various reaction processes within the analyser and makes more detailed comparisons with the Monte Carlo model (Sec.0.4.1) possible. It is constructed from 400×500 mm GEM modules of the same type used in BigBite, except that each set of 4 adjacent readout strips is connected to reduce the number of readout channels. This arrangement is also used for the rear tracking elements employed in the polarimeter proposed for G_E^p/G_M^p measurements [6]. The factor-4 decrease in effective granularity will produce a position resolution of $\sim 250 \mu\text{m}$, which is more than adequate for the present experiment.

In the event that a precise calibration of reconstructed scattering angles in the polarimeter using protons is necessary, an additional set of trackers will be installed in front of the analyser array.

The GEM based trackers will have very high counting rate capability. Compared to GEp(5) the present experiment will run at a factor 8 lower luminosity and the polarimeter will sit at more backward angles. Thus we anticipate that the GEM chambers will handle the lower background rates comfortably.

0.3.2.3 The HCAL Hadron Calorimeter

Downstream of the tracker comes a 11×22 array of calorimeter modules [44] (Fig.10). These modules were originally designed for hadron detection in the 10 - 100 GeV range, but Monte Carlo simulations (Sec.0.4.1) have already predicted that they will perform well in the 1.5 - 10 GeV domain. They are formed from a sandwich of Fe and plastic scintillator plates of total thickness 1 m and a Fe-to-plastic thickness (g/cm^2) ratio of 30.6:1. Scintillation light is collected on a wavelength-shifting guide and then piped to a PMT. These modules form the basis of the planned SBS calorimeter HCAL. Their efficiency and resolution for few-GeV incident nucleons is discussed in Sec.0.4.1.2. The time resolution of the COMPASS modules was around 1.5 ns, but this will be improved substantially by using a faster fluorescent dye in the wavelength-shifting guide. In conjunction with new fast PMTs this will provide a shorter pulse rise time and shorter pulse length. Processing of this pulse is performed by flash ADC hardware which has an order of magnitude higher sampling rate than COMPASS. Thus precise time reconstruction of the fast pulse form will be possible.

0.3.2.4 The 48D48 Dipole

The SBS uses a single dipole for magnetic analysis which has an open geometry, meaning that the detector is in direct view of the target. This approach provides

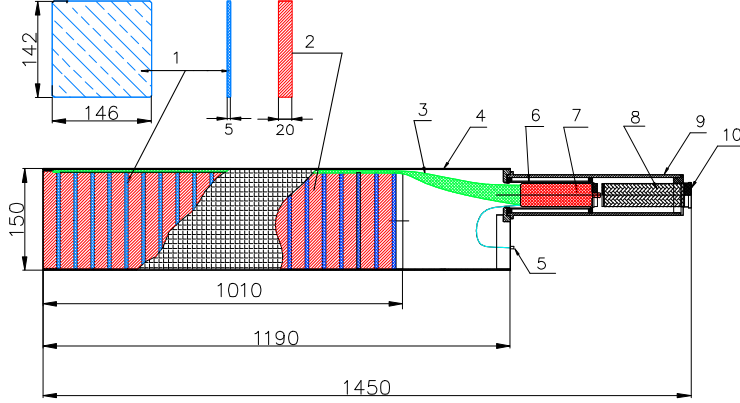


Figure 10: Diagram of a single calorimeter module from Ref.[44]. Components are labeled 1: scintillator sheets; 2: Fe sheets; 3: wavelength-shifting, scintillation readout sheet; 4: metal container; 5: diagnostic optical input; 6: magnetic shield; 7: PMT; 8: PMT HV divider;

a large solid angle and hence improved statistics and of course is suitable for neutron detection.

For quasi-elastic neutron detection the dipole (known as 48D48) has no direct use as a spectrometer, but it serves several purposes:

1. To precess the spin of the recoiling neutron from the longitudinal to the vertical direction. The nucleon polarimeter measures transverse components of spin only.
2. To deflect protons produced in quasi-elastic ${}^2\text{H}(e, e'p)$. These may then be separated from quasi-elastic neutrons through angular correlations with the \vec{q} determined from the electron arm. The vertical deflection, calculated from the reconstructed hit position at the Analyser, is displayed as a function of nucleon momentum, in Fig.11. The incident nucleon angles cover the full vertical acceptance of the 48D48 dipole. Calculations have been made with and without the 50 mm Pb shield. Scattering in the shielding obviously smears the reconstructed-position difference, but with Pb, neutron-proton separation remains good at $p_N = 4$ GeV/c. Without the Pb, proton contamination amounts to $<1\%$ of the neutron signal, while with the Pb it is $\sim 2\%$. Particle identification in the Analyser is augmented by a forward set of 10 mm thick, plastic veto tiles.
3. To sweep low-momentum, charged background out of the acceptance of the polarimeter. The cut-off momentum for charged particles can be gauged from Fig.11. For an integrated field strength of 2 Tm, all charged particles of momenta below ≈ 0.78 GeV/c are swept beyond the Analyzer.

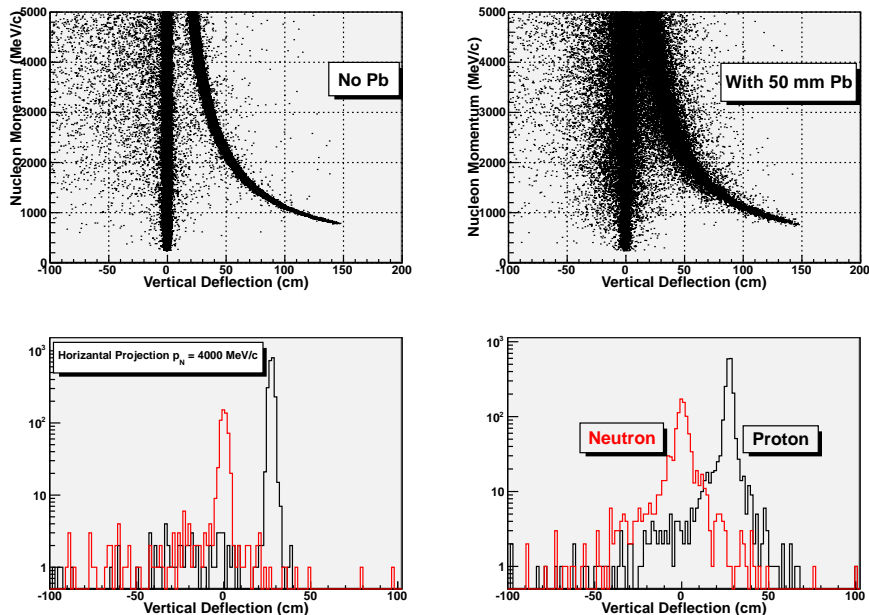


Figure 11: Separation of proton and neutron events

The use of a single dipole spectrometer to precess the spin of the recoil nucleon has the advantage of simplifying the spin transport calculation compared to a multiple-magnet spectrometer such as the HRS.

Simulations of neutron spin precession through the dipole field are currently being verified using parts of the polarimeter Monte Carlo model. Non-perpendicular incidence with respect to the field direction, e.g. due to fringe fields and finite angle range, will produce relatively small rotations in the $z-x$ plane which can affect P_x/P_z and hence G_E/G_M . The initial study will compare the precession through a uniform field, confined to the dipole aperture, with a non-uniform field generated by a TOSCA 3D model of the dipole. This will assess the magnitude of deviations from the ideal case and the sensitivity to different field configurations.

The experimental reconstruction ($\delta\theta_n \sim 5\text{ mrad}$) of the neutron path through the dipole to the analyzer should be good enough to correct for any reasonably smooth, path-dependent variations in precession event by event. The actual field characteristics will be determined after the dipole is installed.

0.3.3 Kinematics

Various kinematic settings have been investigated for $Q^2 = 1.5, 2.0, 2.5, 3.0, 4.0, 5.0$ and 6 (GeV/c)² and are summarized in Table 1. The nominal “central” values of the momenta and angles relate to free $n(e, e'n)$ and the settings in bold-face (Setting 1, 3, 4, 6, 7) are those for which beam time will be requested. Note that the settings at 2.0 and 2.5 (GeV/c)² use a 3.3 GeV beam. If this turns out to be difficult after the CEBAF upgrade, it will be possible to adjust

Setting	Q^2 (GeV/c) ²	E_e (GeV)	$p_{e'}$ (GeV)	θ_e (deg.)	θ_n (deg.)
1	1.5	2.2	1.40	40.8	38.8
2	2.0	2.2	1.14	52.8	31.1
3	2.0	3.3	2.25	29.9	39.7
4	2.5	3.3	1.94	36.7	33.7
5	3.0	3.3	1.70	43.1	29.3
6	3.0	4.4	2.81	28.5	34.7
7	4.0	4.4	2.24	37.3	27.5
8	5.0	5.5	2.82	33.1	26.2
9	6.0	6.6	3.40	30.0	25.0

Table 1: Kinematic Settings. Elastic n(e,e'n) values

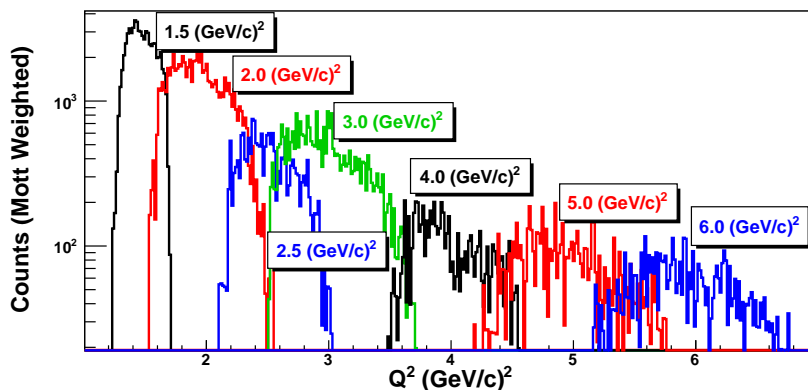


Figure 12: Range of Q^2 for the nominal settings labeled on the plot. The distributions are weighted by the Mott cross section (Eq.5).

the kinematic settings to conform to a CEBAF energy gain of 2.2 GeV per turn. The ranges of kinematic variables for the nominal settings of the large acceptance detector system were calculated for quasi-free ${}^2\text{H}(e, e'n)$ where the internal momentum distribution of the neutron was sampled from $p_N^2 \cdot \exp(-p_N^2/2\sigma_N^2)$, $\sigma_N = 0.03$ GeV/c, i.e. the Fermi distribution was approximated by a Gaussian of width 0.03 GeV/c. Events were generated along the 10 cm length of the target and scattered electrons were detected within the effective 250×750 mm aperture of BigBite situated 1550 mm from the target center. It was also checked if the recoiling neutron is within the acceptance of the 48D48 aperture. BigBite subtends a solid angle of ~ 75 msr and between 50 and 80% of correlated neutrons pass through the aperture of the 48D48. Fig. 12 displays the calculated coverage in Q^2 while the BigBite angular acceptance and $e' - n$ angular correlation for different kinematic settings are shown in Fig.13.

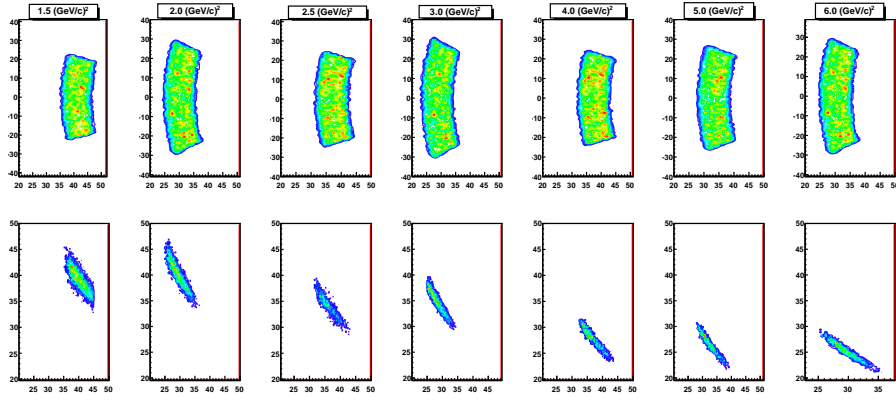


Figure 13: Top row: angular coverage of BigBite, x-axis $\theta_{e'}$, y-axis $\phi_{e'}$. Bottom row $e' - n$ angular correlation, x-axis $\theta_{e'}$, y-axis θ_n .

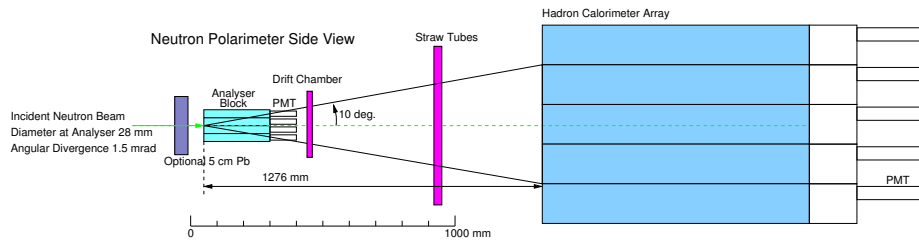


Figure 14: Side view of test polarimeter for analysing power measurements at JINR Dubna.

0.3.4 The Proposed Measurement of the $n - \text{CH}$ Analysing Power at JINR.

The beam time required to achieve a target precision in analysing power (Eq.13,14) depends sensitively on the neutron, organic-scintillator analysing power, which has not been measured at incident momenta of several GeV/c. We propose to measure this quantity [63] at incident momenta of 2, 3.5, 5.0, 6.5 GeV/c using the polarized neutron beam facility of the Nuclotron accelerator at JINR, Dubna.

The device proposed for analysing power measurements in Dubna (Fig.14) is a small-scale version of that planned for a full scale measurement of G_E^n/G_M^n in Hall-A. The individual modules of the analyzer and calorimeter detector arrays are identical, but fewer are required where the incident neutron beam is tightly collimated. A 5 cm-thick Pb wall can be inserted or removed to measure the impact $n + \text{Pb}$ interactions on the polarimeter performance.

The analyzer will consist of a 4×4 array of $40 \times 40 \times 250$ mm bars of EJ-200 plastic scintillator [68], aligned with their long axes parallel to the incident neutron beam. Each bar will be read out by a 19 mm XP1911 PMT.

It is followed by a tracker of the charged particles produced by neutron charge-exchange or hadronic-shower processes within the analyzer. This increases the information obtained on the various reaction processes within the analyzer and makes more detailed comparisons with the Monte Carlo model (Sec.0.4.1) possible. It consists of a 250×250 mm X-Y drift chamber, which has a spacial resolution $\sigma \sim 90 \mu\text{m}$, followed by an array of 64 straw tubes. The latter is arranged in 2×16 tubes, offset by half a diameter and aligned in the X direction, with a similar arrangement aligned in the Y direction. The active area is 600×600 mm.

Downstream of the tracker comes a 5×5 array of calorimeter modules [44] (see Sec.0.3.2.3. These modules were originally intended for detection in the 10 - 100 GeV range, but Monte Carlo simulations (Sec.0.4.1) have already indicated that they perform well in the 2 - 10 GeV domain. They form the basis of the planned calorimeter at JLab.

0.4 Determination of the Ratio G_E^n/G_M^n

The ratio G_E^n/G_M^n will be determined from the scattering asymmetries measured in the recoil neutron polarimeter. The following subsections describe the Monte Carlo simulations of the response of the detector systems, calculations of background rates in the detector systems, the techniques employed to isolate the quasi-elastic signal and finally a discussion of the systematic uncertainties.

0.4.1 Modelling the polarimeter

Monte Carlo simulations [70] of the experiment have been performed within the framework of the the Geant-4 software toolkit. Standard Geant-4 does not consider polarized nucleon scattering and extensions to the hadron-interaction classes have been written, which use fits to previous analyzing power data to

modify the azimuthal distributions of nucleons produced in elastic or quasi-elastic processes. The original code was developed [71] as part of the analysis of the experiment to measure G_{En}/G_{Mn} by recoil polarimetry at Mainz [59].

A brief description of the polarized-scattering model follows:

- Polarization is considered only when the original particle is a nucleon and the material through which tracking is performed contains H or C. Otherwise the standard unpolarized Geant-4 event sampling of azimuthal angle is performed.
- The leading nucleon produced by an elastic or quasi-elastic hadronic reaction process, i.e. with the highest kinetic energy, is identified. If there is no “leading nucleon” the scattering is considered unpolarized.
- The analyzing power for an elastic process is determined on the basis of incident momentum and scattering angle, using a fit to previous experimental data. Several different parametrisations are available for use when sampling azimuthal distributions.
- The rotation in scattering azimuthal angle is sampled with a weighting determined by the transverse component of the incident polarization and the analyzing power.
- This process is repeated if there are multiple elastic scattering events in the analyzer material. In multiple scattering the original reaction plane is lost effectively depolarizing the nucleon.

The geometry and materials of the analyzer block and calorimeter are modeled realistically using standard Geant-4 tools. At this stage the analyser, calorimeter and the 48D48 dipole have been modeled fairly realistically. Electromagnetic interactions are modelled within Geant-4 using the so called extended implementation, while the Hadronic-interactions include:

- Coherent nucleon-nucleon elastic scattering: this method is called for incident energies up to 1.2 GeV. The cross sections are derived from the SAID database.
- Nucleon-nucleus elastic scattering at medium to high energy: the Glauber model is used to calculate differential cross sections for elastic and quasi-elastic nucleon-nucleus scattering. Inelastic screening corrections are implemented at high energy.
- Hadron-nucleus inelastic scattering: this is performed using the so-called Bertini Intranuclear Cascade model. The cascade begins when the incident particle strikes a nucleon in the target nucleus, producing secondaries. These may escape, produce more secondaries or become absorbed. The process continues until all particles with sufficient energy escape the nucleus. This model been tested against data at energies in the range $\sim 0.1 - 5$ GeV.

Monte Carlo data generated by the Geant-4 model were analysed, as if they were real data. The Monte Carlo data stream contains the sensed energies, times etc.

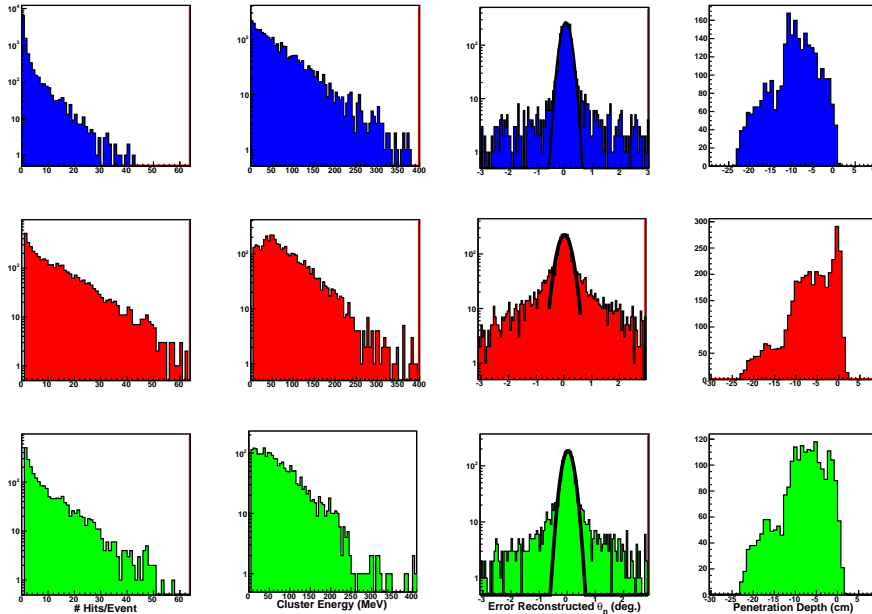


Figure 15: The reconstructed response to 4 GeV/c neutrons of the analyser array. Left to right: number of analyser hits per event, the energy in a reconstructed hit cluster, the error in the reconstructed polar angle and the penetration depth before the 1st hit is registered (the front is at position 0 cm). Blue is no Pb shield, red is with a 50 mm Pb shield, green is with the Pb shield and an anti-coincidence cut on the forward veto scintillator.

from detector elements along with the actual 4-momenta which produce that response. Thus the error distributions in the reconstructed kinematic quantities can be used to assess energy, time and position resolution. Calculations have been made with and without a Pb wall to shield the analyser from the target.

BigBite is partially implemented with the pre-shower, shower and trigger counters in place. A representation of the GEM Chambers is in place, but they are not yet considered in detail. They are modeled in a basic manner as a slab of material with approximately the correct thickness (in terms of g/cm^2) which yields hit positions. These are smeared to a degree consistent with the measured resolution. The properties of BigBite have been proven in a list of recent Hall-A experiments and very detailed Monte Carlo software has been written to simulate 6-GeV configurations which are very similar to the present experiment. The following concentrates on the completely new components of the apparatus on the neutron arm.

0.4.1.1 The Simulated Response of the Analyser Block

Simulated neutrons of momentum 4 GeV/c were incident at specific points of the analyzer. Their interactions within the analyser block produce multiple detector hits per event and “clusters” of hits are reconstructed to produce a cluster energy, hit time and a (\sqrt{E} weighted) mean position. A cluster is constructed after

E_{th}	5	20	40	60	80	100
ε	26.4	21.2	16.0	12.1	9.0	6.9
ε_{Pb}	22.6	19.1	15.0	11.1	8.2	6.0

Table 2: Effective neutron efficiency (%) of the $40 \times 40 \times 250$ mm analyzer array for $p_n = 4$ (GeV/c) and ascending values of the threshold energy E_{th} (MeV). ε_{Pb} is the value with a 50 mm lead shield inserted before the analyzer. Polarimeter calculations have been made with an analyzer threshold of 20 MeV.

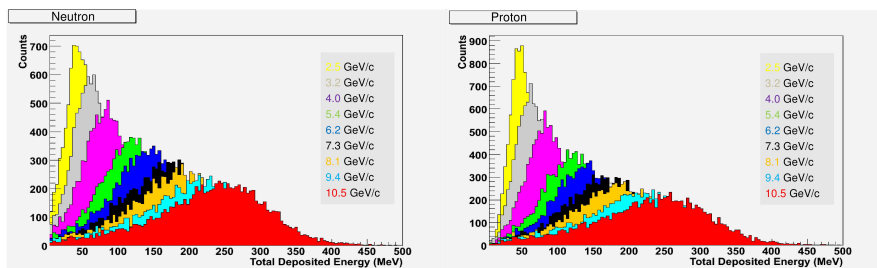


Figure 16: HCAL pulse height response to neutron (left) and protons (right).

finding a detector element with a maximum in energy deposit and then scanning for a signal in the 5×5 array with this element at the center. Timing resolution is discussed in Sec.0.3.2.1.

Calculations have been made for detector elements of 30×30 , 40×40 and 50×50 mm cross section and lengths of 250 mm and 500 mm. Calculations have also been made with a 50 mm Pb wall placed in front of the analyzer array and with a set of 1 cm thick plastic scintillator “veto tiles” placed directly in front of the analyzer. Fig.15 (top row/blue) displays some parameters for 40×40 cm elements with no Pb or scintillator before the array. Gaussian fits to the error (σ) in the reconstructed angle $\delta\theta_n$ produce $\delta\theta_n = 0.12^\circ$, 0.17° , 0.21° for bar cross sections 30×30 , 40×40 and 50×50 mm respectively. Introducing the Pb wall Fig.15 (middle row/red) results in scattering and charged conversion of significant numbers of incident neutrons. There is now a front peak in the penetration depth distribution and greater hit multiplicity. In this case $\delta\theta_n = 0.22^\circ$ and the distribution has more pronounced non-Gaussian “wings”. The situation is improved if a prompt anti-coincidence condition is placed on the prompt timing peak from the forward plastic scintillator, giving $\delta\theta_n = 0.18^\circ$.

The effective detection efficiency, the fraction of incident neutrons which register a hit in the analyzer, is given in Table2. With the veto-tile anticoincidence requirement the effective efficiency is reduced slightly when the Pb wall is in place. Angular resolution calculations were made with a cluster threshold of 20 MeV which corresponds to a detection efficiency of $\sim 20\%$. Counting rates in the analyzer are discussed in Sec.0.4.2.

0.4.1.2 The Simulated Response of the Hadron Calorimeter HCAL

The response of HCAL was also calculated using the simulation, outlined above, and calculations [72] of the response made for the SBS G_M^n proposal [5] are

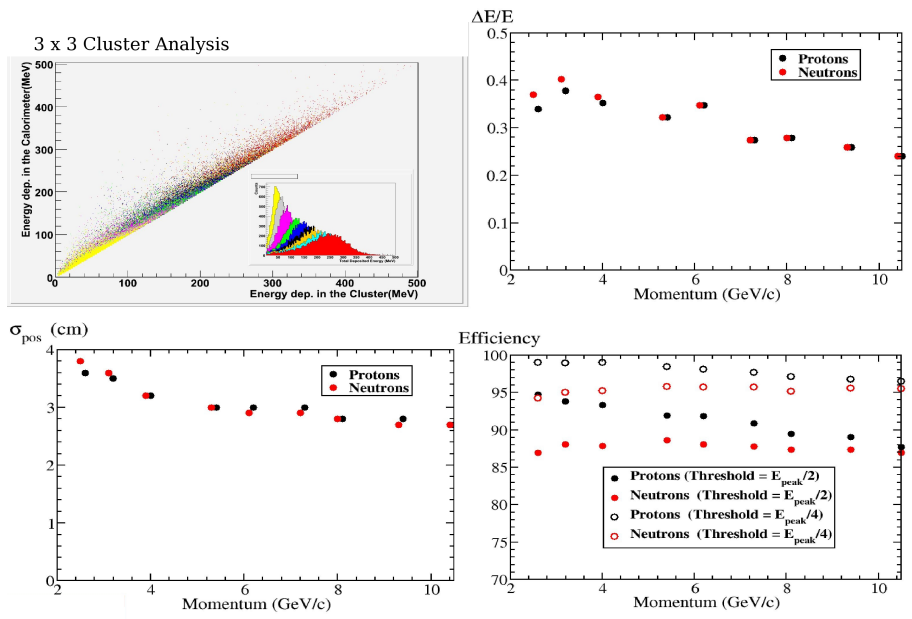


Figure 17: Calculations of HCAL response. Top left: energy leakage from a 3×3 hit cluster; top right: fitted energy resolution of the peak region of the pulse height response (Fig.16); bottom left: position resolution from cluster mean position; bottom right: detection efficiency for 2 threshold settings.

displayed in Fig.16 and 17. These calculations were made without any material (except air) in the path of the incident neutrons. The procedure to reconstruct the HCAL response is very similar to that described in Sec.0.4.1.1. It is clear that the response to neutrons and protons is very similar, with the energy scale in Fig.16 showing the energy loss in the plastic scintillator sheets only. This analysis was made on the assumption that a cluster of hits does not extend beyond a 3×3 group, which results in a small leakage of energy outside of this group. The peaked response means that thresholds can be set high to suppress low energy background from the experimental trigger, without large reductions in detection efficiency. A position resolution of around 30 mm results in a resolution for the reconstructed scattering angle of around 12 mr, which is sufficient for selection of “good” scattering angles where the analysing power is high (Sec.0.4.1.3).

0.4.1.3 The Simulated Response of the Polarimeter

Analysis of the polarimeter response involves reconstruction of the hits in the Analyzer and HCAL, followed by reconstruction of the polar and azimuthal components of the scattering angle. The scattering asymmetry is then obtained from sine (P_x) or cosine (P_y) fits to the azimuthal distribution. Any unpolarized variation in azimuthal acceptance is subtracted before the fit is made.

The effects of finite size and imperfect reconstruction of the scattering process have been investigated using the Monte Carlo model. Multiple scattering in the

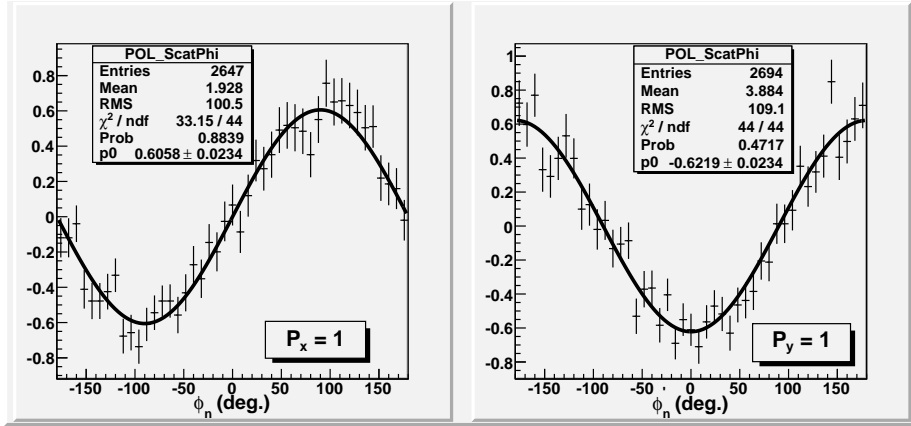


Figure 18: Fits to the simulated azimuthal scattering distributions in the polarimeter for incident polarization $P_{x,y} = 1$ and $A_y = 1$.

A_z (mm)	$A_{x,y}$ (mm)	Pb (mm)	HCAL Thr (% Peak)	ε (%)	D_x $\theta'_n = 1 - 10^\circ$	D_y $\theta'_n = 1 - 10^\circ$
250	30	0	50	7.2	0.68 ± 0.07	0.62 ± 0.06
250	40	0	50	7.6	0.70 ± 0.07	0.78 ± 0.07
250	50	0	50	7.8	0.72 ± 0.07	0.69 ± 0.07
250	30	50	50	6.5	0.50 ± 0.07	0.62 ± 0.07
250	40	50	50	6.9	0.60 ± 0.02	0.62 ± 0.02
250	50	50	50	7.1	0.61 ± 0.07	0.66 ± 0.07
500	40	0	50	14.1	0.62 ± 0.05	0.70 ± 0.05
500	40	50	50	11.2	0.61 ± 0.02	0.62 ± 0.02

Table 3: Systematic variations of dilution effects in the polarimeter. A_z , $A_{x,y}$ are respectively the length and transverse size of the Analyzer bars, Pb is the thickness of the lead shield, HCAL Thr is the threshold setting in HCAL, ε is the calculated polarimeter detection efficiency after selection of angles and $D_{x,y}$ are the dilution factors for incident $P_{x,y} = 1$.

analyzer effectively depolarizes the neutrons as the original reaction plane is lost, but the analyzer also requires to be sufficiently thick that a reasonable efficiency is maintained. Assuming that, as in the case of protons [50], the optimum analyzing power is obtained if the transverse momentum $P_t = P_N^{inc} \sin \theta_N \sim 0.3$ GeV/c, the optimum scattering angle θ_N will drop from 9 to 4 deg. as momentum rises from 2 to 4 GeV/c. The present geometry of the analyzer and HCAL produces a scattering angle resolution of $\sim 0.7^\circ$, which is adequate, and obviously the separation distance can be tuned to suit the scattering kinematics.

Investigations have focused initially on dilution effects in the neutron polarimeter. For this the incident neutrons have been assigned $P_{x,y} = 1$ and the analysing power set to 1. Calculations have been made at an incident momentum of 4 GeV/c, with the analyser threshold set to 20 MeV and the HCAL threshold set at 50% of the peak channel in the pulse-height distribution.

Table 3 lists the Monte Carlo calculated dilution parameters, which are just

the amplitudes of the sine or cosine fits, for different analyzer geometries. The depolarising effects of scattering in the Pb shield appear to reduce $D_{x,y}$ slightly. Stretching the Analyzer to 500 mm length increases the detection efficiency without any apparent large reduction in $D_{x,y}$.

Higher precision calculations are also proceeding with angle and momentum dependent parametrizations of the analyzing power, which should be more sensitive to depolarizing effects. Provisionally an analyser thickness of 250 mm has been chosen (Sec.0.3.2.1).

0.4.1.4 Determination of G_E^n/G_M^n from Simulated Azimuthal Asymmetries

A simulation has also been made using values of P_x and P_z derived from the fit to $G_E^n(Q^2)$ and $G_M^n(Q^2)$ in Ref.[20] and an $n + CH$ analyzing power $A_y^n(p_n, \theta'_n)$ which depends in incident momentum and scattering angle. The estimate of the $n + CH$ analyzing power is based on extrapolations from measured neutron scattering from plastic scintillator (Fig.7). Ref [51] measured an optimum $A_y^{\max} \sim 0.4$ at $p_n = 0.63$ GeV/c for (\vec{n}, n) and a corresponding $A_y^{\max} \sim 0.1$ for (\vec{n}, p) . In the case of $p + CH_2$ scattering [50], the maximum analyzing power may be related to the incident momentum $A_y^{\max} = \kappa/p_p^{\text{lab}}$ $\kappa \simeq 0.4$. The corresponding relation for $p + C$ scattering was $\kappa \simeq 0.36$. Fits to free-nucleon, elastic scattering data [46] yield $\kappa \simeq 0.73$ for $p + p$ in good agreement with [49]. For $n + p$ Ref.[46] suggests $\kappa \simeq 0.78$ although the fit to $n + p$ is less linear than $p + p$. Extrapolating $p + p$ down to 0.63 GeV/c yields a value of $A_y^{\max} \sim 0.6$. Assuming that $n + n$ scattering is also linear in $1/p_n^{\text{lab}}$ and scaling by the neutron-proton analysing power ratio at 0.63 GeV/c, we hypothesize that for $n + n$, $\kappa \sim 0.4 \times 0.4/0.6 = 0.27$.

This of course is speculative and for the present calculation $A_y^n(p_n, \theta'_n)$ we employ the empirical fit of Ref.[50] to $p + CH_2$ data, scaled by the factor 0.4 which we believe is a conservative assumption.

Calculations have been made for 4 combinations of the effective neutron polarizations in the x and y directions: $P_x^* = A_y^{\text{eff}} P_e P_x$ and $P_y^* = A_y^{\text{eff}} P_e P_z \sin \chi$, where A_y^{eff} is the effective analyzing power, $P_{x,z}$ are the x and z components of the recoil neutron polarization, calculated from [20], P_e is the electron beam polarization (0.80) and χ is the angle of precession from $z \rightarrow y$ (Table5). Describing the azimuthal distribution as

$$F(\phi'_n) = C\{1 \pm |P_x^*| \sin \phi'_n \pm |P_y^*| \cos \phi'_n\}$$

then the four possible \pm combinations are labelled F_{++} , F_{--} , F_{+-} , F_{-+}

They mimic the four combinations of beam helicity flip ($P_{x,y}^* \rightarrow -P_{x,y}^*$) and the change of polarity of the 48D48 dipole ($P_y^* \rightarrow -P_y^*$) and may be used to separate the (relatively small) x component from the y . The unpolarized background and x, y components are given by:

$$C = (F_{++} + F_{--} + F_{+-} + F_{-+})/4, \quad (17)$$

$$F_{x1} = (F_{++} - F_{-+})/2C, \quad F_{x2} = (F_{+-} - F_{--})/2C$$

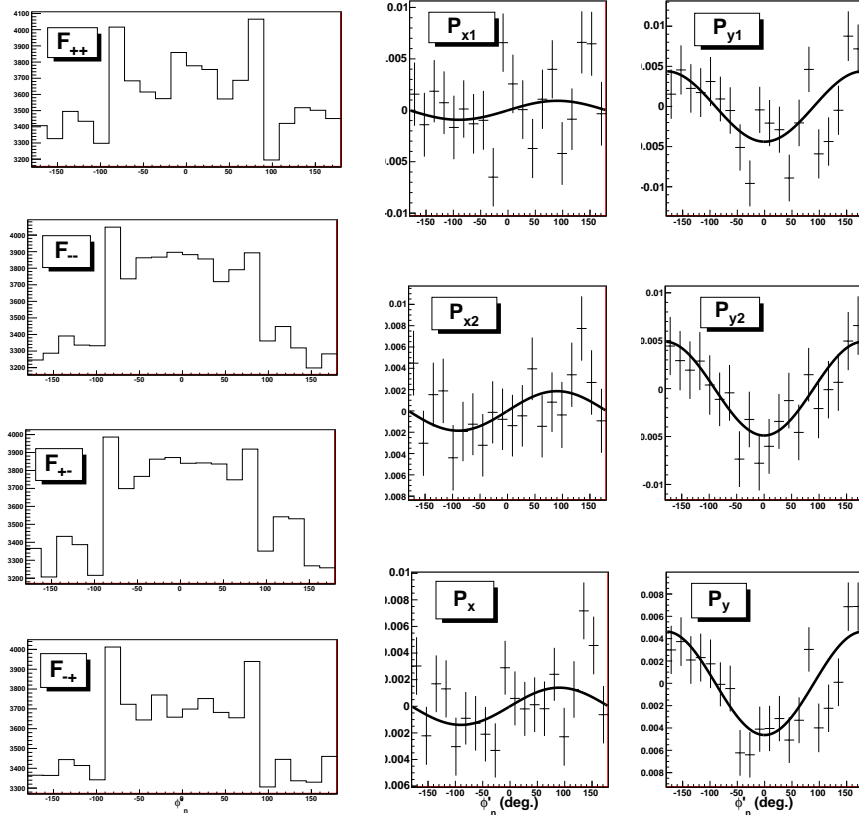


Figure 19: Simulated azimuthal asymmetries generated using “best guess” values of A_y^{eff} and $P_{x,y}^*$. Left: “raw” azimuthal distributions (note the zero is suppressed). Right: fits to separated distributions F_x , F_y (Eq.17). The bottom row right shows the averages of $F_{x1,2}$ and $F_{y1,2}$.

$$F_{y1} = (F_{++} - F_{+-})/2C, \quad F_{y2} = (F_{-+} - F_{--})/2C$$

$F_{x,y}$ are then fitted with sine and cosine functions to obtain the values of $P_{x,y}^*$ and their uncertainties $\delta P_{x,y}^*$. From this is derived the estimated relative precision $\delta R/R$ of the ratio $R = G_E/G_M$.

$$\frac{\delta R}{R} = \sqrt{\left(\frac{\delta P_x^*}{P_x^*}\right)^2 + \left(\frac{\delta P_y^*}{P_y^*}\right)^2} \quad (18)$$

Fig.19 shows simulated azimuthal scattering distributions made with $P_x^* = \pm 0.1$, $P_z^* = \pm 0.45$ and $A_y^{eff}(p_n, \theta_n')$ calculated as described above. The incident momentum p_n was 3 GeV/c, slightly above that of the $Q^2 = 4 \text{ (GeV/c)}^2$ kinematic setting and the total number of incident neutrons simulated was 4×10^6 . The ratio of P_x^*/P_y^* was derived from the sine and cosine fits to the scattering distributions and is displayed in Table 4. The derived value is consistent with that input to the calculation and the relative uncertainty $\delta R/R = 0.5$ is consistent

P_{x1}^* $\times 10^{-3}$	P_{x2}^* $\times 10^{-3}$	P_{y1}^* $\times 10^{-3}$	P_{y2}^* $\times 10^{-3}$	P_x^* $\times 10^{-3}$	P_y^* $\times 10^{-3}$	R_1	R_2	R
0.92	1.85	-4.39	-4.89	1.39	4.63	0.21	0.38	0.30
± 0.93	± 0.93	± 0.94	± 0.93	± 0.66	± 0.66	± 0.21	± 0.20	± 0.15

Table 4: P_x^*/P_y^* Ratio values at an incident momentum of 3.0 GeV/c (bottom row). The input value of R was 0.22.

with the simple prediction ($\delta R/R = 0.49$) of Eq.14 for 4×10^6 incident neutrons. The analysis selected reconstructed, polar-scattering angles in the range $1 - 10^\circ$. The Monte Carlo simulation currently lacks the statistical precision to make quantitative statements about the reliability of a simple estimate (Eq.14) when computing expected uncertainties. Significant improvement in the simulated uncertainty requires batch-farm computing power, which is being setup in Glasgow. Bearing in mind that uncertain analysing power has a large effect on the computed precision, our tentative conclusion is that Eq.14,13 provide a reasonable approximation when assessing necessary counting time.

0.4.2 Background Rates and the Trigger Rate

Singles rates in detectors have been evaluated using the code DINREG [73], which is well proven in estimating background rates in Hall-A. Fig. 20 displays calculated rates for BigBite, made for the present experiment at $Q^2 = 1.5 - 4.0$ (GeV/c)². The shower-counter trigger threshold will be set at around 0.65 of $E_{e'}$ for elastic scattering, which accounts for the range of Q^2 covered by BigBite and also for the momentum resolution. At the settings pertinent to $Q^2=4$ (GeV/c)²: $E_{beam} = 4.4$ GeV, $\theta_{e'} = 37.3^\circ$, $\Omega_{e'} = 78$ msr, $\mathcal{L} = 2.5 \times 10^{38} \text{cm}^{-2}\text{s}^{-1}$, the BigBite trigger rate is estimated at 53 kHz. Thus a coincidence with the neutron arm is necessary for triggering purposes.

Fig. 21 shows equivalent calculations for the neutron arm detectors, made with an integrated field strength of 1.7 Tm which will sweep charged particles of momenta $\lesssim 650$ MeV/c out of the analyzer acceptance. On the left are the rates in the analyzer array for a marginally higher luminosity than the present, and with the analyzer slightly closer to the target. The trigger level (in MeV electron equivalent) and the rate refer to individual scintillator bars. Note that calculations in previous technical sections are also in electron equivalent units, which account for a non-linear pulse height response from non-relativistic particles. For the present case the rate in individual analyzer bars for a threshold of 5 MeV will be ~ 0.1 MHz which is reasonable for a fast plastic scintillator, but rather high to be immediately useful for trigger purposes.

On the right of Fig.21 is the combined rate in a 4×4 cluster of HCAL modules, where the detector geometry is very similar to the present, but the luminosity is double the present value. For incident neutrons of ~ 3 GeV/c the trigger threshold will be ~ 30 MeVee (1/2 of the peak value in the pulse height distribution) and the cluster rate 100 kHz, which translates to a total rate of 1.5 MHz.

With 53 kHz in BigBite, 1.5 MHz from HCAL and a coincidence window of 50 ns the accidental rate will be ~ 4 kHz. This may yet prove to be uncomfortably high for the DAQ system. With improved fast photon-electron selection in the

GEN-Recoil BigBite Trigger Rates vs. Threshold, $\Omega = 60 \text{ msr}$

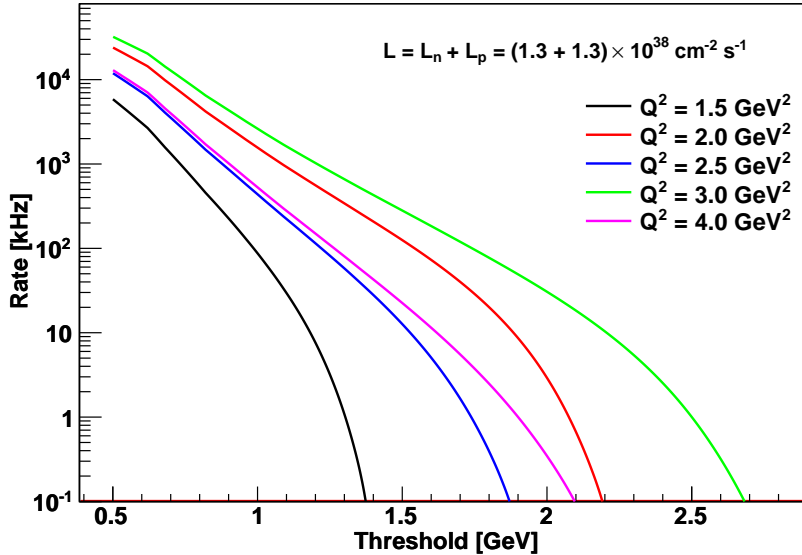


Figure 20: BigBite rate calculations for the present kinematic settings at $Q^2 = 1.5 - 4.0 \text{ (GeV/c)}^2$.

BigBite trigger, the rate could be reduced significantly. We will investigate the use of a GEM chamber placed in front of the BigBite shower counter. This GEM, with fast pixel readout, would have good electron efficiency but low photon efficiency so that photon background would be suppressed. A fast signal would be derived directly from the $5 \times 5 \text{ cm}$ pads of the GEM readout board, which could be correlated using FPGA hardware to the Pb-glass blocks behind.

Based on rates observed in drift chambers during the GEN(1) experiment, a $5 \times 5 \text{ cm}$ pad would, in the present experiment, run at around 1.25 MHz. 50 ns resolution correlations between 400 pads and 189 Pb-glass shower counters would be made in a FPGA based trigger filter, which is part of the SBS apparatus. This would reduce the rate to $\sim 1 \text{ kHz}$, which would be well within the capabilities of the present DAQ system.

Offline analysis selection, via track reconstruction, Cherenkov coincidence requirement and cuts on W , will reduce the BigBite rate considerably. The offline coincidence resolution will be around 10 ns which leads to a $\sim 1\%$ probability of registering an accidental on the neutron arm.

0.4.3 The Quasi-elastic Signal and Background Rejection

Inelastic processes, largely associated with pion electroproduction, and quasi-elastic ${}^2H(e, e'p)$ constitute potential sources of background to the quasi-elastic ${}^2H(e, e'n)$ signal. Contamination of the electron-arm, quasi-elastic event sample by charged pions is expected to be extremely small. Background processes such as pion photoproduction will be suppressed very effectively by offline cuts and should not constitute a significant source of contamination. For the nu-

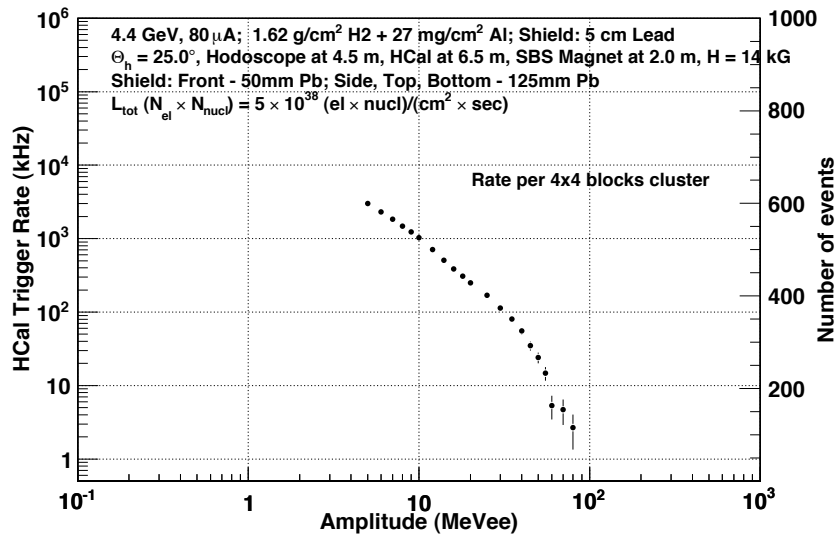
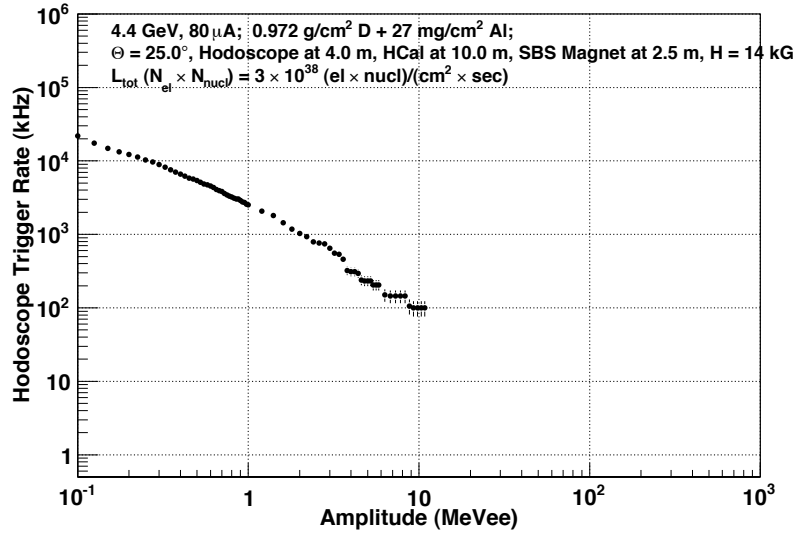


Figure 21: Counting rates in the polarimeter. Top for the analyzer array, bottom for HCal.

clean momenta of interest here, quasi-elastic neutrons may be separated cleanly from the equivalent protons, which are deflected by the 48D48 dipole magnet before incidence on the polarimeter (Sec.0.3.2.4). Based on experience gained on the GEN(1) experiment E02-013 [8], selection of quasi-elastic events from the inelastic background is made on the basis of cuts on

- $p_{miss}^{\perp}, p_{miss}^{\parallel}$, the perpendicular and parallel components of missing momentum, obtained from the neutron momentum \vec{p}_n , provided by the polarimeter hit position and time of flight, and the 3-momentum transfer \vec{q} , provided by BigBite. They are given by: $p_{miss}^{\perp} = |(\vec{q} - \vec{p}_n) \times \vec{q}| / |\vec{q}|$ and $p_{miss}^{\parallel} = \vec{q} \cdot (\vec{q} - \vec{p}_n) / |\vec{q}|$.
- W the invariant mass of the system comprising the virtual photon and the target neutron (assumed free and at rest), given by:

$$W = \sqrt{m_n^2 + 2m_n(E_e - E_{e'}) - Q^2}.$$
- The missing mass in the hadronic final state also gives some additional selection capability.

The W and p_{miss} resolution of the present system has been estimated, using the position and momentum resolutions of BigBite and the polarimeter described in Sec.0.3.

To Summarize: the resolution of the current apparatus in reconstructing these variables was estimated on the basis of assumptions about the angular resolution (σ) of BigBite ($\delta\theta_e = 1$ mr), the momentum resolution of BigBite ($\delta p_n/p_n = 0.5\%$), the (start) time resolution of BigBite ($\delta t = 0.25$), the angular resolution of the analyzer ($\delta\theta_n = 3.5$ mr) and the time of flight resolution of the analyzer (Sec.0.3.2.1). Variations in flight path due to target length and detector thickness are accounted for and the intrinsic PMT time resolution was estimated at 0.3 ns (σ). The calculation considers Fermi smearing of the quasi-free scattering process as in Sec.0.3.3.

The present calculated distributions are compared with real data from GEN(1) (Fig.22). The present p_{miss}^{\parallel} is somewhat poorer at high momentum (bearing in mind that it is at slightly higher momentum), while the p_{miss}^{\perp} distributions appear broadly similar on a 2D plot. The present W distribution for ^2H (as opposed to ^3He in GEN(1)) is tighter.

The calculated 1D distributions of W, p_{miss}^{\perp} and p_{miss}^{\parallel} are compared for $Q^2 = 1.5$ and 4.0 (GeV/c) 2 in Fig.23. . As Q^2 and the momentum of the recoil neutron increases, the resolution from time of flight degrades and with it the resolution of p_{miss}^{\parallel} . BigBite resolution gives a relatively small contribution to the widths of the distributions. The present p_{miss}^{\perp} distributions are confined to $p_{miss}^{\perp} < 0.15$ GeV/c, while the GEN(1) distribution has a significant tail extending to higher missing momenta.

While calculations proceed to evaluate the inelastic contribution, the expectation is that the present experiment will have cleaner quasi-elastic selection capability (based mainly on p_{miss}^{\perp} and W) than GEN(1).

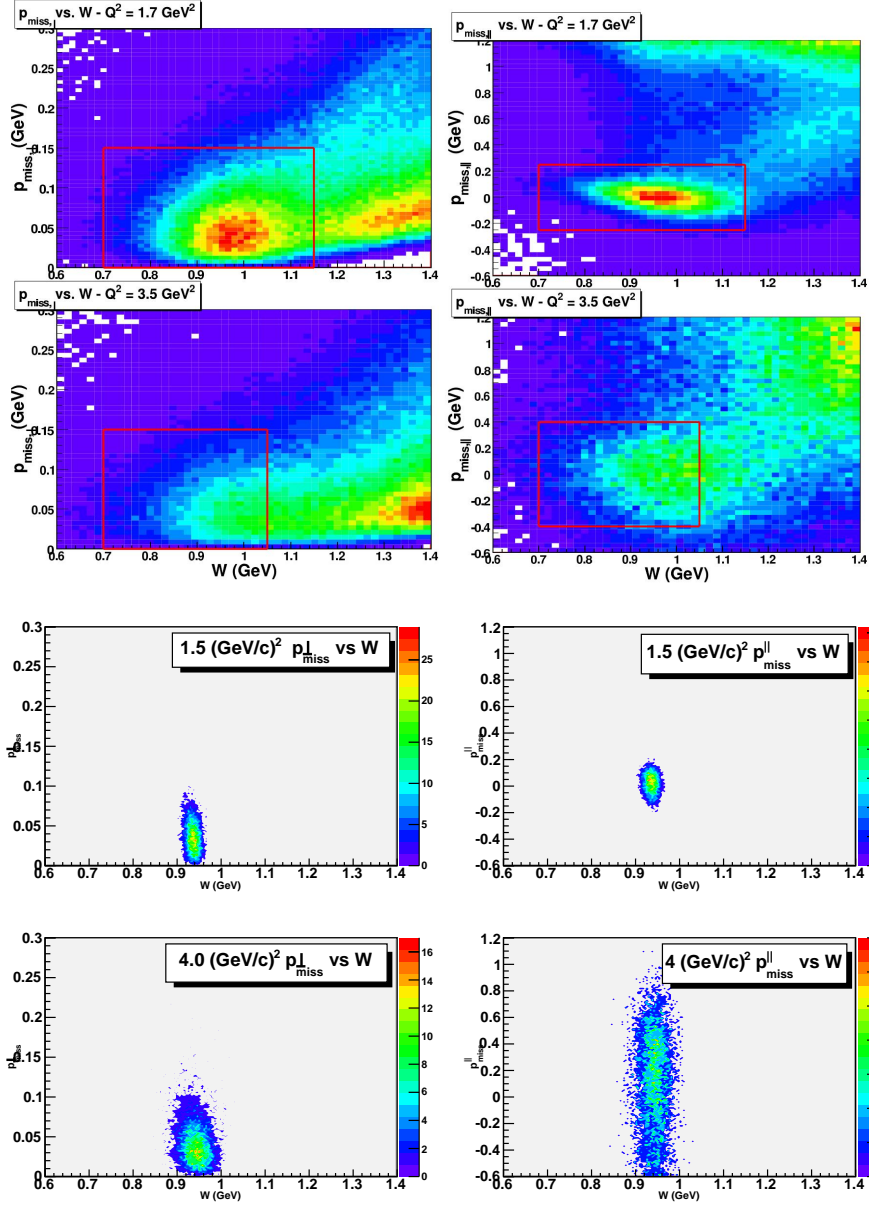


Figure 22: Top plots Left: P_{miss}^\perp and Right: P_{miss}^\parallel vs. W from experiment E02-103. The top row is for $Q^2 = 1.7 \text{ (GeV/c)}^2$, while the second row is for 3.5 (GeV/c)^2 . The bottom plots show present calculations for $Q^2 = 1.5 \text{ (GeV/c)}^2$ and 4.0 (GeV/c)^2 in a similar sequence.

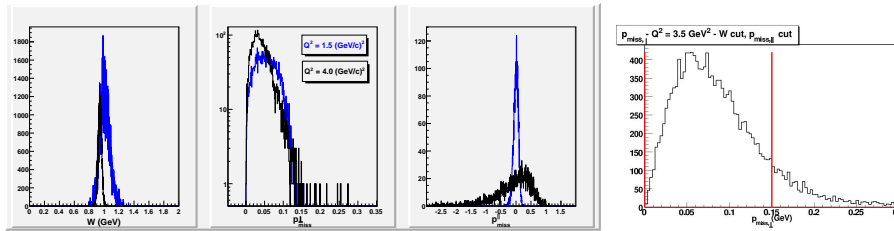


Figure 23: Left: simulated invariant Mass and missing momentum distributions at $Q^2 = 1.5 \text{ (GeV/c)}^2$ (blue) and $Q^2 = 4.0 \text{ (GeV/c)}^2$ (black). Right: p_{miss}^\perp distribution from GEn(1).

0.4.4 Systematic Uncertainties

Some potential major issues associated with analysis of the systematic uncertainties are presented here. Work is in progress to quantify the systematics with more detailed calculations. We expect that more quantitative results will be presented at the PAC meeting.

Potential sources of experimental systematic error are :

- Beam polarization uncertainty, which cancels in a ratio measurement.
- Analysing power uncertainty, which cancels in a ratio measurement.
- Azimuthal angle acceptance non-uniformity, which cancels after beam helicity flip and the additional check of precession angle flip.
- Variation in the effective analysing power with azimuthal angle. The first calculations described in Sec.0.4.1.3 do not show any significant variations. However potential variations in the effective analysing power, which may be different in the x and y directions, as one scans over the full vertical and horizontal range of the analyser, are not ruled out. If this proves to be a significant effect, then it can be corrected if the reconstruction of the scattering angle in the polarimeter is reliable. This can be checked with protons, using the GEM trackers between the analyser and HCAL and an additional front tracker placed before the analyzer.
- Separation of P_x from P_z does not rely on variation of the magnitude of the spin-precession magnetic field. In the present experiment P_x and P_z are measured simultaneously with the same precession field, so that potential effects of changes to the background counting rates on the measured asymmetry are thus avoided.
- Reproducibility of the spin precession angle after polarity reversal. At a precession angle of $\sim 75\%$, a 1% difference in integrated field would give 0.25% difference in $P_z \rightarrow P_y$.
- The vertical distribution of counting rates in the polarimeter will change when the polarity of the spin precession dipole is reversed. Any significant effect from changes to the level of signal contamination should in principle show up when different combinations of beam-helicity-flip and dipole flip asymmetries are compared (Sec. 0.4.1.4).

- Variation in the angle of spin precession through the dipole magnet. The path of a neutron through the dipole can be reconstructed with sufficient precision that a correction factor can be evaluated event by event. The estimate is 0.25%.
- Dilution of the asymmetry by accidental background. The background is estimated to be at the 1% level (Sec.0.4.2) which can be subtracted without significant error.
- Contamination of the quasi-elastic signal by inelastic processes. In GEN(1) the uncertainties in evaluating the inelastic background were estimated as 1.1%, 2.7%, 6.0% at $Q^2 = 1.7, 2.8$ and 3.4 $(\text{GeV}/c)^2$ respectively. A deuteron measurement will have cleaner rejection of the inelastic background. An provisional estimate of 2% is made.
- Dilution of the asymmetry due to proton charge exchange (mainly in the Pb shield) upstream of the veto detectors of the analyzer array. This factor will be evaluated using data from ^1H , ^3He and ^{12}C targets. In GEN(1) the associated systematic uncertainty was between 3 and 4%. Here protons will be deflected by a dipole magnet (Fig.11) before interaction in the Pb wall and thus resultant neutrons will tend to be displaced outside of quasi-elastic data cuts. We estimate a 1% uncertainty provisionally.

Overall we estimate that a 3% systematic error is achievable.

0.5 Proposed Measurements

0.5.1 Counting Rate Estimates

The estimate of required counts is based on the following:

1. The expected degree of polarization of the incident electrons. Previous measurements indicate that values in excess of 0.8 are generally available and we use the value 0.8 for the following estimates.
2. The acceptance of BigBite and the polarimeter for quasi elastic $^2\text{H}(e, e'n)$. The kinematic settings are given in Sec.0.3.3.
3. The predicted detection efficiency and acceptance of the polarimeter is based on Monte Carlo studies. The neutron detection efficiency of the analyzer will be around 20%, while the hadron calorimeter has an efficiency of around 80% for both p and n. The calculations are described in Sec.0.4.1.3. The overall efficiency of the polarimeter, after scattering angle selection, is around 7%.
4. The estimate of the $n + CH_2$ analyzing power has been obtained using the procedure described in Sec.0.4.1.4. Polarimeter figure of merit and uncertainties have been obtained from Eq.13,14 which provide predictions consistent with the results of a simulation of polarized neutron scattering.

Q^2	$\langle p_n^{lab} \rangle$	$\langle P_e P_x \rangle$	$\langle P_e P_z \rangle$	$\langle A_y \rangle$	χ°	F^2 $\times 10^{-4}$	δP $\times 10^{-3}$
1.5	1.44	0.110	0.54	0.087	83	5.28	4.5
2.0	1.76	0.094	0.45	0.077	79	4.20	5.1
2.5	2.05	0.108	0.54	0.069	76	3.39	5.7
3.0	2.35	0.094	0.46	0.062	75	2.71	6.4
4.0	2.89	0.110	0.58	0.051	73	1.79	7.8
<i>5.0</i>	<i>3.43</i>	<i>0.104</i>	<i>0.56</i>	<i>0.041</i>	<i>72</i>	<i>1.17</i>	<i>9.7</i>
<i>6.0</i>	<i>4.03</i>	<i>0.099</i>	<i>0.54</i>	<i>0.032</i>	<i>72</i>	<i>0.72</i>	<i>12.3</i>

Table 5: Values of polarization parameters for incident neutron momenta of interest. The angle brackets denote mean values integrated over the kinematic range of a particular setting. δP values are quoted for 10^7 neutrons detected in the polarimeter, equivalent to 1.43×10^8 incident neutrons. N.B. beam time is not requested for $Q^2 = 5$ and 6 (GeV/c)².

$\langle Q^2 \rangle$ (GeV/c) ²	$\langle \Omega_{e'} \rangle$ (msr)	$\langle \Omega_{e',n} \rangle$ (msr)	$\langle \sigma_n(\theta) \rangle$ (pb/sr)	Rate (Hz)	Time (hr)	$\delta R/R$	
						(stat)	(sys)
1.5	78	59	884	460	2×8	0.029	0.03
2.0	75	38	699	234	2×16	0.038	0.03
2.5	77	59	145	75.5	2×64	0.032	0.03
3.0	74	43	139	52.7	2×120	0.037	0.03
4.0	78	72	17.8	11.3	2×256	0.056	0.03
<i>5.0</i>	<i>75</i>	<i>65</i>	<i>8.5</i>	<i>4.87</i>	<i>2×512</i>	<i>0.079</i>	<i>0.03</i>
<i>6.0</i>	<i>75</i>	<i>67</i>	<i>4.5</i>	<i>2.66</i>	<i>2×512</i>	<i>0.144</i>	<i>0.03</i>

Table 6: Counting rate and error estimate for $n(e, e'n)$ for an incident (neutron) luminosity of $1.26 \times 10^{38} \text{ cm}^{-2}\text{s}^{-1}$. The angle brackets denote averaging over the acceptance of the detector system. “Rate” is the detected $n(e, e'n)$ rate which accounts for solid angle and detection efficiency. N.B. beam time is not requested for settings at $Q^2 = 5$ and 6 (GeV/c)².

Table 5 displays parameters relevant to the precision of the polarization measurement for neutron momenta (p_n^{lab}) associated with $Q^2 = 1.5, 2.0, 2.5, 3.0, 4.0, 5.0$ and 6 (GeV/c)² kinematic settings. The estimate of δP (Eq.14) has been made using the figure of merit F^2 , for 1.43×10^8 incident neutrons, equivalent to 10^7 neutrons detected by the polarimeter. F^2 is calculated (Eq.13) using an efficiency of 0.07, produced by the Monte Carlo simulation (Sec.0.4.1.3), and the parametrisation of analysing power $A_y^n(p_n, \theta'_n)$ described in Sec.0.4.1.4. The parameters P_x^*, P_y^* are calculated from the form-factor fit of Ref.[20] and the efficiency is calculated after selection of polar scattering angle in the range $1 - 10^\circ$.

The time necessary to achieve 10^7 counts can be obtained from the detection rates displayed in Table 6.

The counting rate estimate (Table 6) is based on the expected luminosity and the cross section for free $n(e, e'n)$ scattering. The cross section has been calculated using Eq.5 and the parametrization of the Q^2 dependence of the Sachs form factors of Ref. [20]. A 10 cm LD₂ target has a thickness of 1.69 g/cm²

which gives a (neutron) luminosity of $1.26 \times 10^{38} \text{ cm}^{-2} \cdot \text{s}^{-1}$ for an incident beam current of $40 \mu\text{A}$. The Counting rate estimate assumed a polarimeter efficiency of 7%. The statistical uncertainty is estimated from Eq.18, where δP is given in Table 5. The systematic uncertainty of 3% is discussed in Sec.0.4.4.

0.5.2 Beam Time Request

Beam time is requested (Table 7) to measure G_E^n/G_M^n at five values of Q^2 . The request also includes time for calibrations of the spectrometers and changes in spectrometer positions for different kinematic settings. Electron beam helicity flip is performed at 30 Hz so that combination with the up-down polarized data will yield the effectively unpolarized azimuthal distributions in the polarimeter. At each Q^2 point we will measure at two equal, but opposite polarity setting of the spin-precession dipole. This will effectively reverse the P_y (precessed from P_z), to make the separation procedure of x and z (precessed to y) components of the recoil-neutron polarisation more robust and provide an extra check on possible instrumental effects.

In order to determine the four-momentum of the virtual photon to best accuracy, the optics of BigBite has to be well known. For each kinematic setting data will be taken with a multi-foil carbon target and a removable sieve slit of lead located at the front face of the magnet. These provide the means to calibrate accurately the angular coordinates before magnetic deflection and also the scattering vertex position. The momentum calibration is obtained from elastic $e - p$ scattering from a LH_2 target, where the kinematics are very similar to the quasi-elastic $e - n$ case so that detectors do not require to be moved. Data will also be taken with a liquid ^3He target. In conjunction with the data taken with the other employed targets (^1H , ^2H , ^{12}C) this will facilitate the evaluation of $p - n$ conversion effects.

In total we request 1320 hr of CEBAF beam time. This is broken down in Table 7.

0.6 Summary

We propose to measure the ratio G_E^n/G_M^n from a double-polarization asymmetry using the longitudinally polarized CEBAF electron beam and a polarimeter to measure the transfer of polarization to the recoiling neutron in quasi-elastic $n(\vec{e}, e' n)$. The measurement will be made at five values of the squared four-momentum transfer of the scattered electron $Q^2 = 1.5, 2.0, 2.5, 3.0$ and 4.0 $(\text{GeV}/c)^2$ and will aim to achieve a relative uncertainty (statistical + systematic) in the ratio G_E^n/G_M^n of between 4 and 6%. Systematic effects for recoil polarimetry with an unpolarized deuteron target can be evaluated to good accuracy (provisional estimate 3% uncertainty) and the use of a highly efficient polarimeter results in excellent precision (3 – 5%).

As well as providing an independent check of other G_E^n/G_M^n measurements using polarized-target techniques, this level of accuracy will exercise very powerful constraints on the form factor behaviour at moderate Q^2 . Fig.24 displays the separated d quark ratio $\kappa_d^{-1} F_2^d/F_1^d$ up to 4 $(\text{GeV}/c)^2$, with the impact of the present estimated uncertainties shown as red bars. Clearly the present data

Q ²	Function	Target	Precession	Time (hr)
1.5	Production $^2H(\vec{e}, e'\vec{n})$	LD ₂	pos	8
1.5	Production $^2H(\vec{e}, e'\vec{n})$	LD ₂	neg	8
1.5	BB Optics, Vertex	C Foil	-	24
1.5	Calib. $^1H(e, e'p)$	LH ₂		8
1.5	Calib. $^3He(e, e'p)$	L ³ He		8
1.5	Config Change	-		16
2.0	Production $^2H(\vec{e}, e'\vec{n})$	LD ₂	pos	16
2.0	Production $^2H(\vec{e}, e'\vec{n})$	LD ₂	neg	16
2.0	BB Optics etc.	C Foil		24
2.0	$^1H(e, e'p)$	LH ₂		16
2.0	Calib. $^3He(e, e'p)$	L ³ He		16
2.0	Config Change	-		16
2.5	Production $^2H(\vec{e}, e'\vec{n})$	LD ₂	pos	64
2.5	Production $^2H(\vec{e}, e'\vec{n})$	LD ₂	neg	64
2.5	BB Optics etc.	C Foil		24
2.5	$^1H(e, e'p)$	LH ₂		24
2.5	Calib. $^3He(e, e'p)$	L ³ He		24
2.5	Config Change	-		16
3.0	Production $^2H(\vec{e}, e'\vec{n})$	LD ₂	pos	120
3.0	Production $^2H(\vec{e}, e'\vec{n})$	LD ₂	neg	120
3.0	BB Optics etc.	C Foil		24
3.0	$^1H(e, e'p)$	LH ₂		24
3.0	Calib. $^3He(e, e'p)$	L ³ He		24
3.0	Config Change	-		16
4.0	Production $^2H(\vec{e}, e'\vec{n})$	LD ₂	pos	256
4.0	Production $^2H(\vec{e}, e'\vec{n})$	LD ₂	neg	256
4.0	BB Optics etc.	C Foil		24
4.0	$^1H(e, e'p)$	LH ₂		24
4.0	Calib. $^3He(e, e'p)$	L ³ He		24
4.0	Config Change	-		16
Total				1320

Table 7: Breakdown of beam time request

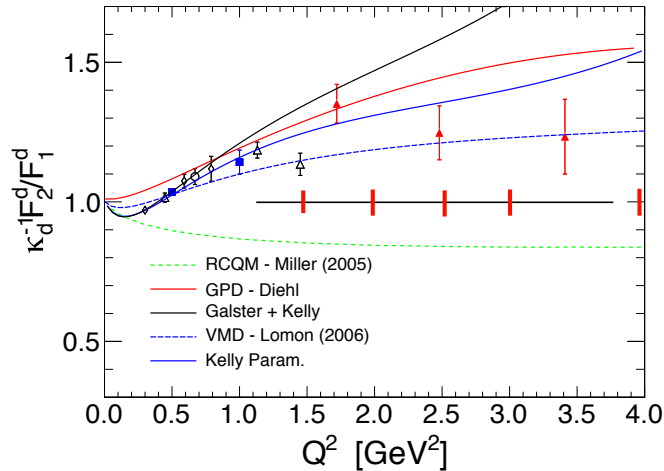


Figure 24: The ratio $\kappa_d^{-1} F_2^d / F_1^d$ as a function of Q^2 . The red bars on the line $\kappa_d^{-1} F_2^d / F_1^d = 1$ display the estimated total uncertainties in the d -quark ratio which would arise from the presently proposed G_E^n / G_M^n measurements.

would represent a major advance in constraining form factor behaviour at moderate momentum transfer, where the sensitivity to structural effects such as the pion-cloud, or di-quark configurations would be most pronounced.

It is very tempting to attempt to extend the range of Q^2 . However, bearing in mind that G_E^n / G_M^n by recoil polarimetry in quasi-free $n(e, e'n)$ has not been measured previously beyond 1.5 (GeV/c)^2 , it is of immense importance to establish the ratio in the $\lesssim 4 \text{ (GeV/c)}^2$ region. Recoil neutron polarimetry is relatively unknown territory in terms of the neutron analysing power of organic materials. We have thus limited our beam request to $Q^2 \leq 4 \text{ (GeV/c)}^2$ where we are confident that good precision can be achieved in a reasonable time. In parallel we propose to measure neutron analysing powers at JINR Dubna, which will firm up our appreciation of the feasibility of higher Q^2 measurements.

The Collaboration

This experiment will be performed in Hall-A of Jefferson Laboratory and approval from Hall-A will be sought retrospectively after submission. It will also be part of the SBS programme of experiments and thus will rely heavily on the apparatus which is being developed jointly for this project. For the present experiment we list the institutes which are most directly involved.

- **Jefferson Laboratory:**

The Hall A group will take on the design of the apparatus layout, the modification of the 48D48 magnet and beam-line vacuum pipe. The group will be responsible for the installation and commissioning of the upgraded infrastructure required for the magnet, the targets, the beam line and the BigBite electron spectrometer. JLab are leading negotiations with SLAC regarding transfer of photomultipliers, originally used for BaBar.

- **University of Glasgow:**

The University of Glasgow have initiated R&D on the polarimeter and have 1 Ph.D. student working full time on this investigation. They will be responsible for electronics and data readout hardware from the analyser array and also for building a small prototype array for measurements at Dubna.

- **JINR Dubna:**

The Dubna group will lead the effort to measure the analysing power of neutron scattering from plastic scintillator at neutron momenta of several GeV/c, using the polarized neutron beam produced by the Nuclotron accelerator in Dubna. They will ensure the necessary provision of beam and infrastructure to carry out the measurement. Dubna are responsible for construction of the modules of HCAL the hadron calorimeter and will supply HCAL modules for the analysing power measurement.

- **INFN Rome:**

The Rome group are leading the effort to build the front tracker GEM chambers and also the design and implementation of the GEM readout electronics. This work is performed within the broader context of the SBS collaboration and benefits all experiments which use the common apparatus.

- **University of Virginia:**

The UVA group are leading the effort to build the large rear GEM chambers and are also heavily engaged in chamber R&D work. This work is performed within the broader context of the SBS collaboration and benefits all experiments which use the common apparatus.

- **Carnegie Mellon University:**

The CMU group lead the R&D effort on the hadron calorimeter modules, which involves optimization of the pulse height response and improvement of time resolution. This work is performed within the broader context of the SBS collaboration and benefits all experiments which use the common apparatus.

- **INFN Catania:**

The Catania group will participate in the R&D and assembly work on the polarimeter.

Cost Estimate of the Polarimeter Analyzer

The major new piece of apparatus required by this proposal is the array of plastic scintillators which form the active analyzer block of the neutron polarimeter. The array consists of 864 bars of plastic scintillator. The realization of this array is planned as follows.

- New plastic scintillator bars would cost \$51,000. Alternatively Glasgow have a stock of large blocks of plastic, used formerly as large time of flight counters. The cost of cutting and machining these into small analyzer bars has been quoted at \$36,000.

- Veto counter scintillator and light guides would cost in the region \$20,000
- The PMT's would be tubes employed previously on the DIRC systems of BaBar. There are in excess of 10^4 of these PMT's and transferring some of them to JLab is the subject of negotiations between the managements of JLab and SLAC.
- The PMT voltage divider, anode pulse fast amplifier and timing discriminator would be guided by a design by the Glasgow group for the detector of the photon tagging spectrometer in Mainz. In this detector plastic scintillator rates in excess of 2 MHz are handled and a time resolution of < 200 ps achieved. If all three functions are implemented on a single circuit board the cost per channel will be \sim \$30, leading to a total cost (analyzer + veto) of around \$33,000. It may be possible to reduce this amount, save space and reduce cabling complexity by grouping 16 sets of amplifier and discriminator circuits on a single circuit board.
- Analogue to digital conversion (both pulse height and time) will use existing hardware within the Hall-A and SBS collaborations.
- The mechanical mounting, including the provision to incorporate shielding is estimated to cost \$7,500.

Bibliography

- [1] R. Hofstadter, Rev. Mod. Phys. 28(1956)
- [2] J.J. Kelly, Phys. Rev. C66(2002), 065203.
- [3] G.A. Miller, Phys. Rev. Lett. 99(2007), 112001.
- [4] *Measurement of the Neutron Electromagnetic Form Factor Ratio G_E^n/G_M^n at High Q^2* , JLab Experiment E12-09-016, Spokespersons: G. Cates, S. Riordan, B. Wojtsekhowski.
- [5] *Precision Measurement of the Neutron Magnetic Form Factor at to $Q^2 = 18$ (GeV/c) 2* . Jefferson Lab experiment E12-09-019, Spokespersons: R. Gilman, B. Quinn, B. Wojtsekhowski,
- [6] *Large Acceptance Proton Form Factor Ratio Measurements at 13 and 15 (GeV/c) 2 Using Recoil Polarization Method*, JLab Experiment E12-07-109, Spokespersons: E. Brash, E. Cisbani, M. Jones, C.F. Perdrisat, L.P. Pentchev, V. Punjabi, B. Wojtsekhowski.
- [7] *Precision Measurement of the Proton Elastic Cross Section at High Q^2* , JLab. experiment E12-07-108, Spokespersons: J. Arrington, S. Gilad, B. Moffit, B. Wojtsekhowski.
- [8] S. Riordan et al., arXiv:1008.1738, Jefferson Lab experiment E02-013, *accepted for publication Phys. Rev. Lett.*
- [9] B. Plaster et al., Phys. Rev. C73(2006),025205.
- [10] M.K. Jones et al. Phys. Rev. Lett. 84(2000), 1398.
- [11] S.J. Brodsky, G.R. Farrar, Phys. Rev. D11(1975), 1309.
- [12] O. Gayou et al., Phys. Rev. Lett. 88(2002),092301.
- [13] V. Punjabi et al., Phys. Rev. C71(2005),055202.
- [14] A. Puckett et al., Phys. Rev. C104(2010),242301.
- [15] L. Andivahis et al., Phys. Rev. D50(1994),5491.
- [16] M.E. Christy et al., Phys. Rev. C70(2004),015206.
- [17] I.A. Qatten et al., Phys.Rev.Lett. 94(2005)142301.

- [18] A.V. Belitsky, X. Ji and F. Yuan, Phys. Rev. Lett. 91(2003), 092003.
- [19] B. Wojtsekhowski, Private Communication, Nov. 2010.
- [20] J.J. Kelly, Phys. Rev. C70(2004),068202.
- [21] C.D. Roberts and A. G. Williams, Prog. Part. Nucl. Phys. 33(1994), 477.
- [22] I.C. Cloët et al., Few Body Syst., 46(2009), 1.
- [23] E.L. Lomon, Phys. Rev. C66(2002),045501.
- [24] E.L. Lomon, arXiv:nucl-th/0609020, September 2006.
- [25] R. Bijker and F. Iachello, Phys. Rev. C69(2004),068201.
- [26] G.A. Miller, Phys. Rev. C66(2002), 032201 R.
- [27] C.D. Roberts et al., Eur. J. Phys. ST 140(2007),53.
- [28] H.H. Matevosyan, A.W. Thomas and G.A. Miller, Phys. Rev. C72(2005),065204
- [29] M. Diehl et al., Eur. J. Phys. C39(2005),1.
- [30] M.R. Frank, B.K. Jennings and G.A. Miller, Phys. Rev. C54(1996), 920.
- [31] G.A. Miller and M. R. Frank, Phys. Rev. C65(2002), 065205.
- [32] M. Gockeler et al., (QCDSF/UKQCD), PoS LAT2007(2007),161, arXiv:0710.0422 [hep-lat].
- [33] H.W. Lin et al., arXiv:1005.0799v1 [hep-lat], 5th May 2010.
- [34] X. Ji, Ann. Rev. Nucl. Part. Sci. 54(2004), 413.
- [35] A.V. Belitsky and A.V. Radyushkin, Phys. Rep. 418 (2005).
- [36] X. Zheng et al. Phys. Rev. C70(2004), 065207.
- [37] A. Airapetian et al., Phys. Rev. Lett. 94(2005),012002.
- [38] V. Yu. Alexakhin et al., Phys. Rev. Lett. 94(2005),202002.
- [39] *Measurement of the Single Target-Spin Asymmetry in Semi-Inclusive $\vec{n}(e, e'\pi^-)$ Reaction on a Transversely Polarized Target*, JLab Experiment E06-010, Spokespersons: J.-P. Chen, X. Jiang, J.-C. Peng.
- [40] *Target Single Spin Asymmetry in Semi-Inclusive Deep-Inelastic $(e, e'\pi^+)$ Reaction on a Transversely Polarized ^3He Target*, JLab Experiment E06-011, Spokespersons: E. Cisbani, H. Gao, X. Jiang.

- [41] A. Adare et al. Phys. Rev. D76(2007), 051106(R).
- [42] A.I. Akhiezer et al., JEPT 33(1957),765.
- [43] R.G. Arnold et al., Phys. Rev. C23(1981),36
- [44] N.V. Vlasov et al., Instr. and Exp. Tech. 49(2006),49.
- [45] R. Diebold et al., Phys. Rev. Lett. 35(1975),632.
- [46] *Analysing Power of pp and np Elastic Scattering at Momenta between 2000 and 6000 GeV/c and Polarimetry at LHE*, V.P. Ladygin, JINR report E13-99-123, 1999.
- [47] A. de Lesquen et al., Eur. J. Phys. C11(1999),69
- [48] CNS Center for Nuclear Studies, SAID Partial Wave Analysis, R. Arndt et al., <http://gwdac.phys.gwu.edu/>.
- [49] H. Spinka et al., Nucl. Instr. and Meth. A211(1983),239.
- [50] L.S. Azhgirey et al., Nucl. Instr. and Meth. A538(2005),431.
- [51] T. Wasaka et al., Nucl. Instr. and Meth. A547(2005),569.
- [52] I. Passchier et al., Phys. Rev. Lett. 82(1999),4988.
- [53] H. Zhu. Phys. Rev. Lett. 87(2001),081801.
- [54] C. Herberg et al., Eur. J. Phys. A5(1999),
- [55] J.Becker et al., Eur. J. Phys. A6(1999),329.
- [56] D.Rohe et al., Phys. Rev. Lett. 83(1999),4257.
- [57] T. Eden et al., Phys. Rev. C50(1994),1749.
- [58] M. Ostrick et al., Phys. Rev. Lett. 83(1999),276.
- [59] D.I. Glazier et al., Eur. J. Phys. A24(2005),101.
- [60] G. Warren et al., Phys. Rev. Lett. 92(2004),042301.
- [61] *The Neutron Electric Form Factor at Q^2 up to 7 (GeV/c) 2 from the reaction $^2\text{H}(\vec{e}, e'\vec{n})$ via Recoil Polarimetry*. JLab. Proposal PR12-09-006, Spokespersons: B.D. Anderson, J. Arrington, S. Kowalski, R. Madey, B. Plaster, A. Yu. Semenov
- [62] *Measurement of analyzing power for the reaction $\vec{p} + \text{CH}_2$ at polarized proton momentum of 7.5 GeV/c*, JINR Proposal ALPOM2, Spokespersons: C.F. Perdrisat, N.M. Piskunov, E. Thomasi-Gustafsson.
- [63] *Measurement of the Analysing Power of Polarized Neutron Scattering on Organic Scintillator at Incident Momenta of Several GeV/c*, JINR PAC Proposal (in preparation), Spokespersons: J.R.M. Annand, N.M. Piskunov, B. Wojtsekhowski.

- [64] J. Lachniet et al., nucl-ex 0811.1716, Phys. Rev. Lett.
- [65] S. Rock et al., Phys. Rev. D46(1992),24.
- [66] *Measurement of the Neutron Magnetic Form Factor at High Q^2 Using the Ratio Method on Deuterium*, JLab experiment E12-07-104, Spokespersons: W. Brooks, G. Gilfoyle, J. Lachniet, M. Vineyard.
- [67] B. Ketzer et al., Nucl. Instr. and Meth. A535(2004),314.
- [68] Eljen Technology, <http://www.eljentechnology.com/>
- [69] *The DIRC Particle Identification System for the BaBar Experiment*, I Adam et al., SLAC-PUB-10516, June 2004.
- [70] *A Geant-4 Based Monte Carlo of SBS*, J.R.M. Annand, University of Glasgow 2010.
- [71] *Measurement of the Neutron Electric Form Factor at $Q^2 = 0.8 (\text{GeV}/c)^2$* , D.I. Glazier, Ph.D. Thesis, University of Glasgow, 2003. <http://www.nuclear.gla.ac.uk/npe-theses>
- [72] *HCAL for SuperBigBite*, F.Benmokhtar, IV SuperBigBite Spectrometer Meeting, JLab, March 19, 2010.
- [73] P.V. Degtyarenko, [23, 24, 25]computer code DINREG, *Applications of the Photonuclear Fragmentation Model to Radiation Protection Problems*, Proc. Second Specialist Meeting on Shielding Aspects of Accelerators (SATIF2), CERN, October 1995